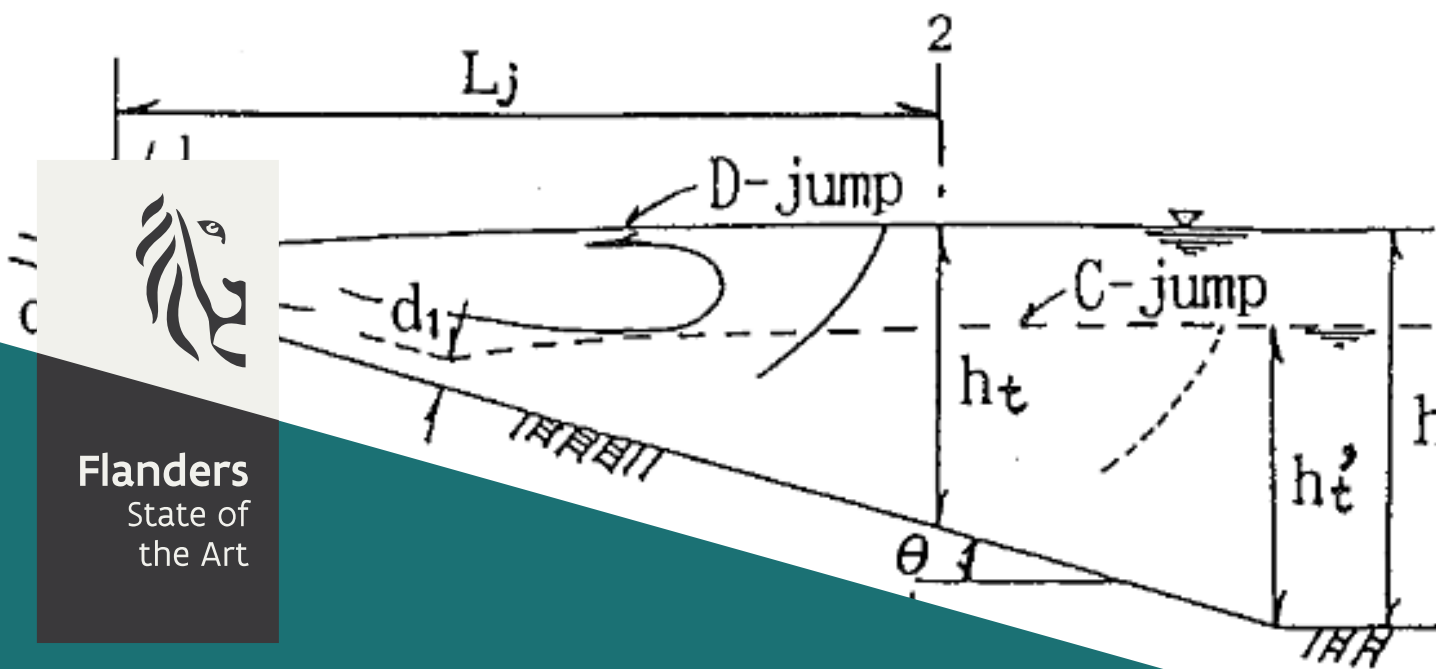


(a)



20\_035\_2  
FH Reports

## On the numerical resolution of hydraulic jumps

Algorithms, Boundary Conditions, and Turbulence  
Models

DEPARTMENT  
MOBILITY &  
PUBLIC  
WORKS

[www.flandershydraulics.be](http://www.flandershydraulics.be)

# On the numerical resolution of hydraulic jumps

Algorithms, Boundary Conditions, and Turbulence Models

López Castaño, S.; van Hoydonck, W.

Legal notice

Flanders Hydraulics is of the opinion that the information and positions in this report are substantiated by the available data and knowledge at the time of writing.

The positions taken in this report are those of Flanders Hydraulics and do not reflect necessarily the opinion of the Government of Flanders or any of its institutions.

Flanders Hydraulics nor any person or company acting on behalf of Flanders Hydraulics is responsible for any loss or damage arising from the use of the information in this report.

Copyright and citation

© The Government of Flanders, Department of Mobility and Public Works, Flanders Hydraulics, 2024  
D/2024/3241/087

This publication should be cited as follows:





**López Castaño, S.; van Hoydonck, W.** (2024). On the numerical resolution of hydraulic jumps: Algorithms, Boundary Conditions, and Turbulence Models. Version 3.0. FH Reports, 20\_035\_2. Flanders Hydraulics: Antwerp

Reproduction of and reference to this publication is authorised provided the source is acknowledged correctly.



Document identification

Customer:	Flanders Hydraulics	Ref.:	WL2024R20_035_2
Keywords (3-5):	hydraulic jump, FVM, RANS, CFD		
Knowledge domains:	Hydraulics and sediment > Hydrodynamics > Waves > Numerical modelling		
Text (p.):	31	Appendices (p.):	9
Confidential:	No	<input checked="" type="checkbox"/> Available online	
Author(s):	López Castaño, S.		

Control

	Name	Signature
Revisor(s):	van Hoydonck, W.	Getekend door:Wim Van Hoydonck (Sign Getekend op:2024-08-05 09:56:15 +02:0 Reden:Ik keur dit document goed  
Project leader:	López Castaño, S.	Getekend door:Santiago LOPEZ CASTA Getekend op:2024-08-09 15:39:14 +02:0 Reden:Ik keur dit document goed  

Approval

Head of division:	Bellaïkih, A.	Getekend door:Abdelkarim Bellaïkih (Sign Getekend op:2024-08-01 14:11:41 +02:0 Reden:Ik keur dit document goed  
-------------------	---------------	--

# Abstract

This report deals with the verification and validation of a newly proposed modification to the  $k-\omega$  SST model and optimized Volume-of-Fluid (VoF) algorithm for the simulation of stable hydraulic jumps in engineering settings. The proposed modifications suggest alternatives to the Scale-Adaptive-Simulation (SAS) concept in order to tackle some perceived deficiencies in the original formulation of Menter and Egorov, 2010, for two-phase incompressible flows incurring in sheared flows. Additional modifications to the proposed turbulence model are suggested in order to reduce spurious generation of turbulence across the interface and close to walls. Results show overall agreement with literature studies regarding the study of hydraulic jumps in sloped channels, including numerical and physical experiments. Furthermore, implicit-explicit *Flux-Corrected Transport* methods are implemented in order to allow the use of dual time-step discretizations.

# Contents

Abstract .....	III
List of Figures .....	V
List of Tables .....	VII
Nomenclature .....	VIII
1 Introduction .....	1
1.1 Why a hydraulic jump? .....	2
1.2 Objectives .....	2
1.3 The use of OpenFOAM .....	2
2 Mathematical Model .....	4
2.1 Governing Equations of flow .....	4
2.2 RAS turbulence model .....	4
2.2.1 The k-omega SST-SAS model .....	5
2.2.2 Towards a better definition of the von Karman length $L_{vk}$ .....	6
2.3 Algorithmic aspects .....	8
2.3.1 Linearization practices in fvSchemes .....	8
2.4 Boundary conditions and stability .....	10
3 Verification and Validation: Hydraulic jump .....	12
3.1 Previous grid-refinement studies: challenges and misconceptions .....	13
3.1.1 Grid Convergence Study: trivial archetype .....	14
3.1.2 Grid Convergence Study: second archetype .....	15
3.2 Validation using A-type (or classical) hydraulic jumps .....	16
3.2.1 Fully developed inflow: verification of the stresses .....	17
3.2.2 Volume-of-Fluid verification: shape of the hydraulic jump .....	19
3.2.3 Dynamics of the flow within the hydraulic jump .....	20
3.2.4 How validate the surface roller length, $L_r$ ? .....	22
3.3 Validation using B-type hydraulic jumps .....	23
3.3.1 Shape of the B-type hydraulic jump .....	24
3.3.2 Internal flow mechanism of the B-Type jump .....	24
3.4 Further insights using B-type hydraulic jumps on steep slopes .....	26
3.4.1 Internal flow character of the B-Type jump in steep slopes .....	27
4 Discussion .....	29
4.1 Future work .....	29
A1 Theoretical Considerations .....	A1
A1.1 Theory, research, and practice of hydraulic jumps .....	A1
A1.2 Onset of flow separation in weak and oscillating hydraulic jumps: basics .....	A4
A1.3 Onset of flow separation in weak and oscillating hydraulic jumps: empirical and numerical evidence .....	A6
References .....	A8

# List of Figures

Figure 1	Sketch of the mean longitudinal flow inside a CHJ. The dotted line represents the shear region between the surface roller and the wall jet. Here, $U$ is velocity and $\alpha$ void fraction. ....	6
Figure 2	Cumulative mass error for two types of boundary conditions at the outlet of an open-channel flow.....	11
Figure 3	Types of hydraulic jumps in sloped channel transitions as theorized by Ohtsu and Yasuda, 1991. Notice that the A-type jump corresponds to a Classical Hydraulic Jumps (CHJ). ....	12
Figure 4	Dam break simulation at $T = 0.5$ s. ....	14
Figure 5	Classic hydraulic jump downstream of a slope with angle $\theta$ : (a) sketch of the problem, (b) numerical domain. ....	15
Figure 6	Time-averaged 1-D profile of cross-section-integrated bottom shear stress for the sloped section of the channel, normalized using the hydraulic jump height $h_j$ . ....	18
Figure 7	Velocity profile of the fully developed supercritical flow in the sloped channel for the outer layer ( $\mathbf{R} > 1000$ ), presented in viscous units. ....	19
Figure 8	Visual inspection of the hydraulic jump's roller length via surface flow patterns using the time-space averaged velocity field. ....	19
Figure 9	Normalized shape of the hydraulic jump. ....	20
Figure 10	Internal flow characteristics of the A-type hydraulic jump for $\mathbf{R}_\tau \approx 17000$ and $\mathbf{F} = 4.68$ . (a) Maximum velocity decay along the axis of the jump, and (b) vertical profiles of velocity at different locations along the axis. ....	21
Figure 11	Various experiments relating the roller length to the Froude number, conducted by various research groups (Peterka, 1964).....	22
Figure 12	Surface flow patterns for a B-type jump. ....	23
Figure 13	Normalized shape of the B-Type hydraulic jump. ....	24
Figure 14	Internal flow characteristics of the B-Type hydraulic jump for $\mathbf{R}_\tau \approx 16500$ and $\mathbf{F} = 4.68$ . (a) Maximum velocity decay along the axis of the jump, and (b) vertical profiles of velocity at different locations along the axis. ....	25
Figure 15	(a) Normalized shape of the hydraulic jump and (b) Surface streamlines for the B-type jump in a steep slope. ....	26
Figure 16	Internal flow characteristics of the B-Type hydraulic jump for $\mathbf{F} = 7.51$ . (a) Maximum velocity decay along the axis of the jump, and (b) vertical profiles of velocity at different locations along the axis. ....	28
Figure 17	Acceleration zone as theorized by Ohtsu and Yasuda, 1991.....	30
Figure 18	Hydraulic jump classification according to the Froude number. ....	A1
Figure 19	Dimensionless surface profiles of hydraulic jumps in horizontal channels, taken from Peterka, 1964. Experiments were conducted originally by Rajaratnam and Subramanya, 1968. ....	A2
Figure 20	Characteristic curves of hydraulic jumps in horizontal rectangular channels (Peterka, 1964). The sub-indices 1 and 2 refer to locations upstream and downstream from the jump, respectively. ....	A3
Figure 21	Contours of (a)-(c) mean streamwise velocity and (b)-(d) Reynolds shear stress of hydraulic jumps over flat beds, from an instantaneous snapshot produced by numerical simulations. Plots (a)-(b) correspond to an oscillating jump while plots (c)-(d) correspond to a stable hydraulic jump. Taken from Jesudhas <i>et al.</i> , 2018.....	A3
Figure 22	Length in terms of sequent depth $y_2$ in horizontal channels. Notice that the suggested range for design is $4.5 < \mathbf{F}_1 < 9$ . Taken from Peterka, 1964. ....	A4

- Figure 23 Control volume, delineated by the black dotted lines, indicating the forces acting on a hydraulic jump in the subcritical region. Notice the upper dotted line represents the outer-most streamline of the surface roller. The circle symbol denotes the end of the surface roller, which enters in contact with the atmosphere. .... A5
- Figure 24 (a) Non-dimensional streamwise time-averaged velocity profiles after the toe of a hydraulic jump, located at  $x_t$ . The solid line represents the velocity profile exactly at the toe,  $(x - x_f)/h_j = 0$ , and each subsequent line correspond to unit increments (1, 2, 3, ...). The triangle symbol shows the location of the free-surface and the arrow indicate the direction of unit increments. (b) Surface streamlines for time- and spanwise-averaged solution of a weak hydraulic jump. The field VF stands for volume-fraction. Taken from Mortazavi *et al.*, 2014. .... A7

## List of Tables

Table 1	Grid convergence history for different Reynolds-Averaged Simulation (RAS) models used in the study of so-called <i>classical</i> hydraulic jumps. For details on the study refer to Bayón <i>et al.</i> , 2019.	13
Table 2	Grid convergence analysis for $r = 2$ using the dam break case. ....	15
Table 3	Grid convergence analysis for $r = 2$ using the hydraulic jump case. A 4th refinement step is done, but not used for the calculation of $p$ . Notice that the metrics for the 4th refinement are not monotonic anymore. ....	16
Table 4	Case study conditions for the sloped channel. ....	17



# Nomenclature

## Abbreviations

CFD	Computational Fluid Dynamics
CHJ	Classical Hydraulic Jumps
EFD	Experimental Fluid Dynamics
FH	Flanders Hydraulics
FOAM	Field Operation And Manipulation library
FOSS	Free- and OpenSource Software
FVM	Finite-Volume Method
PISO	Pressure-Implicit with Splitting-Operator
RANS	Reynolds-Averaged Navier-Stokes
RAS	Reynolds-Averaged Simulation
VoF	Volume-of-Fluid

# 1 Introduction

*An experimentalist is he whom his results everybody believes, except for himself,  
and a “numericalist” is he whom his results nobody believes, except for himself.*

– William Eichinger

Computational Fluid Dynamics (CFD) is the *de facto* tool for the study of transonic reactive flows, thermal hydraulics in nuclear facilities, and in ship hydrodynamics, both in academic and industrial settings, just to name a few use cases. More recently, the area of applicability has expanded to eco-hydraulics, and hydraulic engineering in general. One common feature in the types of flows just described is the inherent difficulty in their study via experiments, mostly due to the limitations present in scale modelling and measurements. These limitations are not exclusive to such fields: hydraulic engineering practice relies heavily on scale modelling, despite its shortcomings when measuring bubbly flows and similarity arguments.

Previous experimental studies conducted by the Author (López Castaño *et al.*, 2021) have elucidated the challenges in measuring flow patterns within a hydraulic jump’s roller with an acceptable accuracy. Phenomena such as aeration and bubble dynamics (coalescence, break-up, entrainment, de-gassing) present in the hydraulic jump make it difficult to measure the structure of turbulence and general flow accurately using classical PIV techniques. An accurate measurement of such type of flows using optical methods require phase-detection probes that synchronize the camera with the bubbly phase. Such complexities make CFD attractive whenever details on the structure of hydraulic jumps are needed.

Thus, in an effort to complement the tools that currently Flanders Hydraulics (FH) uses for the study of flow phenomena in hydraulic structure set-ups (e. g. : locks, fish passages, weirs, dike overflow), validation and verification studies using CFD software are being conducted. A first study performed by De Schrijver, 2021 explored the features of hydraulic jumps after slopes using CFD; it was found, amongst other things, that the results were quite sensitive to the choice of turbulence model and solver settings, even when using sufficiently refined grids.

Given the aforementioned challenges, This work focuses on the extension, development, and validation of a novel turbulence model suitable for the study of flows typical in hydraulic engineering under the RAS philosophy. Additionally, modifications on the traditional VoF and Pressure-Implicit with Splitting-Operator (PISO) algorithms are proposed in order to accelerate the convergence of the solution. Here a round of validations will be performed following the configuration and type of flows studied by De Schrijver, 2021. Namely, the present work emphasizes on the validation of flows involving hydraulic jumps which, typically, are amongst the most ubiquitous features in hydraulic engineering design.

A word of caution: this work will make often use of the words “steep” and “mild” slopes when referring to the vertical gradient of the sloped channel. These words may have different meanings in the context of hydraulic engineering, depending on the topic being studied. Here, the focus is on *Rapidly varied flows*, as opposed to *Gradually varied flows*, more precisely local features regarding hydraulic jumps in sloped channels hence the terms “slope”, “mild”, and “steep” refer to orographic features rather than hydraulic ones. So, when the text mentions a hydraulic jump occurring after a mild slope it should be understood as a hydraulic jump occurring after a channel with a slope  $\theta = 5^\circ$  or less<sup>1</sup>, and not a hydraulic jump happening after an M1/M2 type channel flow (which would be impossible in any case). To be clear, all sloped channels in the present study are *hydraulically steep*.

---

<sup>1</sup>Notice this threshold is defined according to the criterium  $\cos \theta \rightarrow 1$  as  $\theta \rightarrow 0$ .

## 1.1 Why a hydraulic jump?

With the aforementioned precept in mind, a single archetype flow representative of the flows often encountered in eco-hydraulics will be chosen on which this work will be based. This archetype should permit the study of the following aspects:

1. Rapidly-varying open-channel flows: accurate resolution of the free-surface is important.
2. Unsteady-ness: the classical tools of hydraulics are not able to accurately represent unsteady behaviour in transient and non-transient flows.
3. Turbulence: The classical treatment of turbulence in hydraulics (as a force, or stress) is just ignored for rapidly-varied flows. However, internal mechanisms of dissipation may be present which, in principle, can be conveniently expressed in terms of forces. Mathematical descriptions obtained for such kinds of flows are based on potential-flow theory which, in some cases, offer insufficient information regarding the *internal forces* needed for the design of, say, fish passages.

Based on the aforementioned list, it is clear that the archetype flow needed for the analysis should be the hydraulic jump. Hydraulic jumps, or standing waves in general, are ubiquitous in hydraulic engineering practice and are flow features used by practitioners often to their advantage during design. Given the unsteady and turbulent character of hydraulic jumps, and the difficulties in representing and measuring such flows at scale, it becomes an ideal candidate for this study.

## 1.2 Objectives

This report will conduct numerical experiments of interest in hydraulic engineering and eco-hydraulics practice with the intent to:

1. Optimize existing algorithms for the study of high-Reynolds number two-phase flows.
2. Propose and implement a novel turbulence model for the solution of the Reynolds-Averaged Navier-Stokes (RANS) equations.
3. Validate the code implemented against different types of hydraulic jumps using available data and current theory.
4. Propose future research lines based on the experience gained in the present study.

The present report will perform a validation and verification study of some methodologies proposed for the accurate simulation of flows of interest in hydraulics using RAS. This implies that the present validation will not attempt to determine, given the richness of data coming from the present study, whether all aspects of the flow (such as turbulence budget, vorticity dynamics, bulking, etc) are either accurately resolved or modelled. The validation will solely focus on the validation of *ensemble-average* fields and features, and not on higher-order moments nor focus on the physics of mixing and turbulence. It is expected then that the user of the present algorithm understands the limitations of RAS and pseudo-time stepping for the study of inherently unsteady flows, in particular hydraulic jumps, and interpret the results accordingly.

## 1.3 The use of OpenFOAM

The Author has developed during the years on various CFD codes, mostly Free- and OpenSource Software (FOSS), and during his tenure in FH most of his numerics-related work has been conducted using Field Operation And Manipulation library (FOAM), which has at least three known forks. Starting from the assumption that

the underlying libraries are *correct*, that is, that it follows the principles of correctness, reproducibility, abstraction, and stability needed in any parallel code, details on the programming aspects of the codes implemented by the Author will not be given. Code fragments of FOAM may be shown, depending on the context.

The point here is that the use of OpenFOAM, foam-extend, or any other CFD tool or version or fork for that matter, should be considered incidental to the discussion being held here and should bear no implication whatsoever in the conclusions derived from this work.

## 2 Mathematical Model

*Natura non faciat saltus, nec ab extremo ad extremum transeat nisi per medium.*

– John Ray

This chapter describes the governing equations for two-phase incompressible flows using the VoF technique. Additional details will be given regarding the turbulence models and algorithmic aspects intended for making simulations more robust and reliable in the context of hydraulic engineering. A short discussion on boundary conditions will be given as well.

The reader must assume that the derivations herein presented will be linearized within the formalism of the Finite-Volume Method (FVM) which is the technique of choice in many CFD libraries, including FOAM.

### 2.1 Governing Equations of flow

The governing RANS equations of two-phase fluid flow in the context of VoF may be written in the following manner, in indicial notation:

$$\frac{\partial \rho \bar{u}_i}{\partial t} + \frac{\partial \bar{u}_j \bar{u}_i}{\partial x_j} = \frac{\partial \bar{p}_d}{\partial x_i} + \frac{\partial}{\partial x_k} \left( \mu \frac{\partial \bar{u}_i}{\partial x_k} \right) - g_i x_i \frac{\partial \rho}{\partial x_i} + \frac{\partial \bar{u}_i}{\partial x_k} \frac{\partial \mu}{\partial x_k} - \frac{\partial \tau_{ij}^{\text{res}}}{\partial x_j}, \quad (1)$$

$$\frac{\partial \alpha}{\partial t} + \frac{\partial \bar{u}_j \alpha}{\partial x_j} + \frac{\partial \hat{u}_j \alpha (1 - \alpha)}{\partial x_j} = 0, \quad (2)$$

$$\frac{\partial \bar{u}_i}{\partial x_i} = 0, \quad (3)$$

$$p_d = p - \rho g_i x_i, \quad (4)$$

$$\rho = \alpha \rho_{H_2O} + (1 - \alpha) \rho_{air}, \quad (5)$$

$$\mu = \alpha \mu_{H_2O} + (1 - \alpha) \mu_{air} \quad (6)$$

where  $\vec{u} = u_i$  are the cartesian velocities,  $\vec{g} = g_i$  gravity,  $\alpha$  the color (indicator, or so-called volume fraction) function,  $\overline{(\cdot)}$  a temporal filter, and  $\hat{u} = \hat{u}_i$  the interface compression velocity. Pressure-velocity coupling is achieved using PISO. The compression velocity will be described in terms of the local Courant number ( $Co$ ), in the following manner:

$$\hat{u}_i = \frac{1}{2} \frac{n_i^\Gamma |\Delta_i|}{\delta t}, \quad (7)$$

where it is assumed that the ratio between numerical and interface fluxes ( $Co$ ) must always remain below or equal to 0.5, and where  $\vec{n}^\Gamma = n_i^\Gamma$  is the surface normal to the air-water interface  $\Gamma$ ,  $\vec{\Delta} = \Delta_i$  is the distance between two neighbouring centroids that share a face, and  $\delta t$  the time step. This approach differs from the original approach in Ubbink and Issa, 1999, for reasons that will be made apparent in later sections.

### 2.2 RAS turbulence model

This work is focused mainly on large scale processes and simulations of engineering interest in the field of hydraulics, and those particular to hydraulic jumps. In that sense, RAS models will be used throughout this

work, hence the Boussinesq hypothesis for the treatment of the residual fluxes of momentum is used, that is,

$$\tau_{ij}^{\text{res}} = \overline{u_i u_j} - \overline{u_i} \overline{u_j} = 2\mu_{\text{res}} S_{ij} - k\delta_{ij},$$

where

$$S_{ij} = \frac{1}{2} \left( \frac{\partial \overline{u_i}}{\partial x_j} + \frac{\partial \overline{u_j}}{\partial x_i} \right).$$

The rest of this section will focus on ways of modelling the residual viscosity  $\mu_{\text{res}}$ , and for the remaining of this work it is assumed that all velocity fields are time-filtered.

### 2.2.1 The k-omega SST-SAS model

Based on the archetype flow of study (i.e. the hydraulic jump) chosen for the present work, the standard k- $\omega$  SST-SAS closure model (Menter and Egorov, 2005; Menter, 1992) is augmented with a buoyancy production term in the turbulence kinetic energy, or  $k$ , equation; while stabilized closure terms for the specific dissipation, or  $\omega$ , equation are used following recent developments for the study of non-linear waves in incompressible two-phase flows (Devolder *et al.*, 2017; Larsen and Fuhrman, 2018; Umlauf *et al.*, 2003). The governing equations are the following:

$$\frac{\partial \rho k}{\partial t} + \frac{\partial \rho u_j k}{\partial x_j} = \rho P_k - \rho P_b - \rho \beta^* k \omega + \frac{\partial}{\partial x_j} \left[ \left( \mu + \rho \sigma^* \frac{k}{\omega} \right) \frac{\partial k}{\partial x_j} \right], \quad (8)$$

$$\frac{\partial \rho \omega}{\partial t} + u_j \frac{\partial \rho \omega}{\partial x_j} = \rho P_\omega - \rho \beta \omega^2 + \rho \frac{\sigma_d}{\omega} \frac{\partial k}{\partial x_j} \frac{\partial \omega}{\partial x_j} + \frac{\partial}{\partial x_j} \left[ \left( \mu + \rho \sigma \frac{k}{\omega} \right) \frac{\partial \omega}{\partial x_j} \right] + Q_{\text{SAS}}. \quad (9)$$

The residual viscosity may be then calculated as follows:

$$\mu_{\text{res}} = \rho \nu_{\text{res}} = \rho \frac{k}{\tilde{\omega}},$$

where the  $\tilde{(\cdot)}$  over the specific dissipation term means a form of stabilization, or correction, and  $\nu_{\text{res}}$  is the kinematic residual viscosity. The constants  $(\alpha, \alpha_b^*, \beta, \beta^*, \sigma, \sigma^*, \sigma_b)$  are defined elsewhere. The turbulence kinetic energy production term is defined as follows:

$$P_k = \tau_{ij} \frac{\partial u_i}{\partial x_j} = 2\nu_t S_{ij} S_{ij},$$

and the production of specific dissipation is proportional to  $P_k$ :

$$P_\omega = \alpha \frac{k}{\omega} \frac{\tilde{\omega}}{\tilde{\omega}} P_k.$$

where  $\tilde{(\cdot)}$  means another form of wall-model stabilization. Additionally, the production of turbulence kinetic energy due to buoyancy is expressed as follows:

$$P_b = \frac{g_i}{\rho} \overline{\rho' u_i'} = \nu_t \alpha_b^* \frac{g_i}{\rho} \frac{\partial \rho}{\partial x_i}.$$

Finally, the last term on the rhs of Equation 9,  $Q_{\text{SAS}}$ , resolves the smallest (dissipative) scales in the turbulence spectrum, represented by the mesh. In other words this term accounts for the smallest, dissipative, and unsteady features of the flow, hence the importance of this term for the study of CHJ and hydraulic jumps in

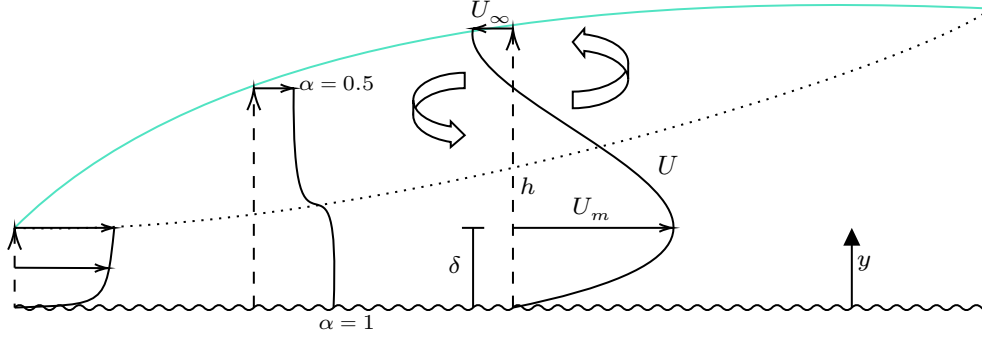


Figure 1 – Sketch of the mean longitudinal flow inside a CHJ. The dotted line represents the shear region between the surface roller and the wall jet. Here,  $U$  is velocity and  $\alpha$  void fraction.

general without resorting to LES. The SAS model of Menter and Egorov, 2010 proposes the following:

$$Q_{\text{SAS}} = \max \left\{ \rho \xi_2 S_{ij} S_{ij} \left( \frac{L}{L_{vk}} \right) - C_{\text{SAS}} \frac{2\rho k}{\sigma_\Phi} \max \left[ \frac{1}{k^2} \left( \frac{\partial k}{\partial x_j} \right)^2, \frac{1}{\omega^2} \left( \frac{\partial \omega}{\partial x_j} \right)^2 \right], 0 \right\}, \quad (10)$$

$$L = \frac{k^{1/2}}{\omega c_\mu^{1/4}}, \quad (11)$$

$$L_{vk} = \kappa S_{ij} \left/ \left| \frac{\partial^2 u_k}{\partial x_k^2} \right| \right. . \quad (12)$$

The standard SAS model may under-predict TKE production for regions with low velocity laplacians but finite vorticity stretching, as will be shown in the following section.

## 2.2.2 Towards a better definition of the von Karman length $L_{vk}$

In order to perform a stability analysis on the steady-state solution of Equations 8 and 9, the mean vertical velocity profile proposed by McCorquodale and Khalifa, 1983 and shown in Figure 1, is used:

$$U = U_m \left( \frac{y}{\delta} \right)^{1/7}, \quad 0 < y < \delta \quad (13)$$

$$U = U_\infty + (U_m - U_\infty) e^{-4c \left( \frac{y-\delta}{h-\delta} \right)^2}, \quad y > \delta \quad (14)$$

where  $U_m$ ,  $U_\infty$ ,  $c$ ,  $y$ ,  $h$ , and  $\delta$  are the maximum velocity, velocity at the free-surface, a constant ( $\approx 0.7$ ), the vertical coordinate, water depth, and boundary-layer thickness, respectively. If one assumes  $\delta \ll h$ , that is, when the Reynolds number of the incoming flow is very high ( $\text{Re} \rightarrow \infty$ ), then one can reduce Equations 13 and 14 to:

$$U_* = e^{-4cy_*} \quad (15)$$

for the entire depth. The non-dimensional velocity  $U_*$  and depth  $y_*$  are defined as:

$$U_* = \frac{U - U_\infty}{U_m - U_\infty}$$

$$y_* = \frac{y}{h}$$

One can easily prove that the von Karman length,  $L_{vk}$ , is singular for the steady-state velocity profile proposed

earlier:

$$\begin{aligned} L_{vk} &= \kappa \left| \frac{\partial U_*}{\partial y_*} / \frac{\partial^2 U_*}{\partial y_*^2} \right|, \\ &= \kappa \left| \frac{y_*}{1 - 8cy_*^2} \right| \rightarrow \infty, \end{aligned} \quad (16)$$

as:

$$y_* \rightarrow \sqrt{\frac{1}{8c}},$$

making  $Q_{SAS} \rightarrow 0$  within the roller region, despite it being a region of vorticity production. In other words, as one reaches a steady-state solution the model will under-predict dissipation within the roller (see Equation 10).

On the other hand, the current definition of  $L_k$  may lead to inconsistent treatment of the production terms present in the turbulence model. More specifically, by averaging in time Equations 8 and 9 in the outer region of the flow, one obtains the following simplification:

$$\begin{aligned} 0 &= \rho P_k - \rho P_b - \rho \beta^* k \omega, \\ 0 &= \rho P_\omega - \rho \beta \omega^2 + Q_{SAS}. \end{aligned}$$

Notice that the production of turbulence kinetic energy and buoyancy is *always* positive, making  $P_b$  a destruction term for  $k$ . For the specific dissipation on the other hand, production of  $\omega$  is mediated by  $Q_{SAS}$  and  $P_\omega$ , which are also positive.

In cases where  $Q_{SAS} = 0$  due to very large velocity laplacians ( $L_{vk} \rightarrow \infty$ ) one finds that the resulting time-integrated turbulence model equations become inconsistent for the jet flow that forms beneath the roller, as shown:

$$\begin{aligned} 0 &= P_k - \beta^* k \omega, \\ 0 &= P_\omega - \beta \omega^2 = \alpha \frac{P_k}{\nu_t} - \beta \omega^2, \end{aligned}$$

from where different expressions for  $P_k$  can be obtained, making the model inconsistent. This calls for a re-definition of the von Karman length scale, which represents better the time-scales associated with vorticity production and dissipation, and guarantees consistency in the turbulence model for hydraulic jumps. A simple alternative is one based on vorticity itself, that is:

$$L_{vk} = \kappa \frac{|\Omega_{ij}|}{\sqrt{\frac{\partial \Omega_{ij}}{\partial x_k} \frac{\partial \Omega_{ij}}{\partial x_k}}}, \quad (17)$$

where  $\Omega_{ij}$  is the skew-symmetric part of the velocity gradient. This is a more natural definition for  $L_{vk}$  compared to the original formulation shown in Equation 16, given the fact that the roller region will always have finite and continuous vorticity profile (Hornung *et al.*, 1995) in the mean.

Notice that in two dimensions Equation 17 reduces to Equation 16, if one uses the self-similar velocity profile proposed in Equation 14. As a consequence, one may conclude that the use of either equation is indifferent for this particular problem. However, this simplification is misleading for two reasons:

1. The maximum vertical-velocity  $V_m$  decays at a rate proportional to  $x^{-3/2}$  following that of the streamwise-velocity  $U'_m \propto x^{-1/2}$  by virtue of mass conservation (Rajaratnam and Subramanya, 1968), thus giving finite vortex-stretching in the direction transversal to the flow. Additionally, by virtue of the dynamic condition at the interface between fluids, the shear stress acting on a curved free surface contributes to the vertical derivatives of vertical velocity, thus making  $u_2 = f(x_1, x_2)$ . In 2DV, the transversal direction is not modelled by definition.



2. Flows with null-valued laplacians are not devoid of vortices, even in two dimensions. Furthermore, a vorticity-production mechanism via surface-reconnection at the toe of the hydraulic jump guarantees non-decaying vorticity in the roller and shear regions in the hydraulic jump (Hornung *et al.*, 1995). In our case, it is obvious that the flow on the roller and shear region has non-zero mean vorticity, hence  $Q_{SAS}$  must contribute to the production of  $k$ , even in 2D.

## 2.3 Algorithmic aspects

The modifications implemented in the  $k-\omega$  SST-SAS turbulence model make the solution more accurate and at the same time more robust, for the following reasons:

1. Classical  $k-\omega$  models with buoyancy correction produce excessive specific dissipation at the air-water interface, even for potential or laminar waves. The inclusion of stabilization terms suggested by Larsen and Fuhrman, 2018 mitigate such over-dissipation, reducing the spurious currents product of over-dissipation.
2. The suggested compression velocity is guaranteed, by definition, not to produce fluxes that will be dominant for the calculation of the Courant number. This is particularly important when simulations are being conducted using local-time stepping.

However, robustness and stability may be improved by realizing the following two assumptions: (1) although flows in hydraulic engineering are bi-phasic, the interest rests on the liquid part of the simulation, and (2) the time scales of interest are invariably inertial.

The first assumption can be tackled by defining a range for  $\alpha$  for which there is no interest; in other words, a region of *pure air*. In the present study, one can define such region as  $\alpha_{air} \in [0, 0.1]$ . A common practice is to clip the velocity to  $\vec{0}$  and set the pressure to hydrostatic within the aforementioned range, but that will produce excessive velocity gradients in cells that undergo changes in  $\alpha$  that span the range from fully dry to fully wet. In those regions, instead, it is preferred to limit the convection of momentum. Like that, one guarantees that the stability in the pure air phase is still given by the diffusive operator (maximum Courant will remain on the water phase) while letting momentum to be diffused only. The modifications to Equation 1 are simple:

$$\frac{\partial \rho u_i}{\partial t} + H(\alpha - 0.1) \frac{\partial \rho u_j u_i}{\partial x_j} = (\dots), \quad (18)$$

where  $H$  is the Heaviside function. This forces the momentum transport and mixing processes to be purely *diffusive* in the air phase, compared to the original RANS equations.

To tackle the second assumption running with high Courant numbers ( $\mathcal{C}_o \gg 1$ ) is an imperative. As it currently stands, the solution of the color function transport equation 2 present in FOAM follows either semi-implicit approach based on MULES (Deshpande *et al.*, 2012), whereby the convective term is treated explicitly using a Flux Corrected Transport (FCT), or a fully explicit geometric VoF reconstruction, scheme. Such schemes are upwinded in nature, thus restricting the application of the MULES model to low Courant Numbers. One may solve equation 2 implicitly instead, and linearize the convection term there using MHRIC schemes (Park *et al.*, 2009).

### 2.3.1 Linearization practices in fvSchemes

The linearization of all mathematical operators are described in Listings 2.1. Details on these operators can be found elsewhere.

---

Listing 2.1 – The fvSchemes used in this work.

---

```

ddtSchemes
{
    default          CoEuler phi rho 0.5;
}
gradSchemes
{
    default          cellLimited leastSquares 1.0;
}
divSchemes
{
    div(rho*phi,U)      Gauss vanLeer;//LUST grad(U);
    div(rho*phi,k)      Gauss limitedLinear 1.0;
    div(rho*phi,omega)  Gauss limitedLinear 1.0;
    div(phi,alpha)      Gauss MHRIC 0.5;
    div(phirb,alpha)    Gauss interfaceCompression;
}
laplacianSchemes
{
    default            Gauss linear corrected;
    laplacian(rUaf,pd) Gauss linear corrected;
}
interpolationSchemes
{
    default            linear;
    interpolate(grad(U)) linear;
}
snGradSchemes
{
    default            corrected;
}

```

Notice that for the time operator the local time stepping linearization was not used. This linearization is commonly used within the context of MULES in OpenFOAM.

The Author has found this scheme to produce too much mass-conservation errors due to the spurious smoothing of  $\alpha$ , as shown in Listings 2.2. This form of local-time stepping does not guarantee propagation of local properties according to the local Courant number. For this reason, CoEuler scheme is preferred.

---

Listing 2.2 – Local-time stepping.

---

```

//- in setRDeltaT.H
    // (...)
    rDeltaT.ref() = max
    (
        1/dimensionedScalar("maxDeltaT", dimTime, maxDeltaT),
        fvc::surfaceSum(mag(phi))()()
        /((2*maxCo)*mesh.V())
    );
    // (...)
    // this function ensures that neighbouring values
    // do not vary more than
    // (1 - rDeltaTSmoothingCoeff) of the 'owner' value
    if (rDeltaTSmoothingCoeff < 1.0)

```

```
{
    fvc::smooth(rDeltaT, rDeltaTSmoothingCoeff);
}
//- in fvcSmooth.C
// Propagate information over whole domain
FaceCellWave<smoothData, smoothData::trackData> smoothData
(
    mesh,
    changedFaces,
    changedFacesInfo,
    faceData,
    cellData,
    mesh.globalData().nTotalCells(), // max iterations
    td
);
```

## 2.4 Boundary conditions and stability

One of the topics that seems to confuse newcomers to CFD for eco-hydraulics is boundary conditions. Here, a short explanation will be given for the choice of boundary conditions for the *momentum* equation 1 and for the color function 2 in the context of open-channel flows.

If the flow is non-transient, that is, the local derivative of mass in the whole domain of integration at all times remains zero, one can perfectly use combinations of Dirichlet and Neumann boundary conditions for the momentum and color equations, respectively, even in the case where the water level at a certain downstream boundary is not presumed.

One common approach for CFD practitioners, even researchers (Macián-Pérez *et al.*, 2020), in this kind of situations is to define so-called *open* boundary conditions at the outlet of their models, even if one may know exactly how much discharge should go through this outlet. This may not be the most effective way to approach such scenarios, in terms of stability, where the total mass balance involves a number of *phases*: any mass error in one phase, well, must be compensated by the other phases<sup>2</sup>. An “open” boundary must enforce mass conservation according to the projection step (which involves a user-defined pressure at this boundary) in the PISO algorithm, and what that step does is to lump all phase-fluxes into one single phase-averaged flux for which the correction is done thus distributing any mass defect or error through all phases, including the water phase. For the Dirichlet boundary condition, error is directly reflected on the water depth but not on the pressure residual.

Setting a Dirichlet outlet is simple: if one knows the the water height and the velocity (discharge) at a particular outlet of the domain<sup>3</sup> one just needs to impose a Dirichlet condition for the velocity equal to the mean velocity of the flow at the outlet<sup>4</sup> and leave the rest of the fields (pressure, color function) with natural boundaries.

Using a Dirichlet instead of an “open” boundary condition works because the relation between water height and velocity in open-channel flows is known a-priori (verified by color transport equation numerically), thus it doesn’t need to be calculated at each iteration (via projection step). Given that solving the Poisson Equation for pressure tends to be more expensive and produces stiffer residual matrices compared to the solution of advection-diffusion equations, it is expected that guaranteeing mass conservation via pressure may lead to

---

<sup>2</sup>Mass errors in VoF simulations come in two forms: (1) time-scale, and (2) length-scale, related. The maximum Courant (< 1) limit for upwinded mass transport is a well known metric used for explaining mass-related errors.

<sup>3</sup>a good practitioner should conduct a simple 1D study prior to a full fledged CFD, anyway

<sup>4</sup>strictly speaking, you have to set the velocities in the air phase to zero, although this is not necessary

stability issues.

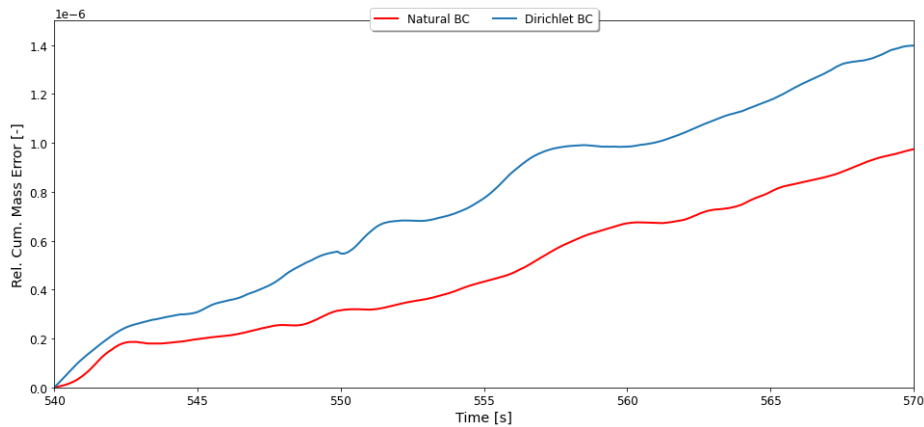


Figure 2 – Cumulative mass error for two types of boundary conditions at the outlet of an open-channel flow.

More specifically, the stability of either type of boundary condition for an outlet can be readily assessed for a 2-D classical hydraulic jump simulation<sup>5</sup>. The initial cumulative mass conservation error, that is, the volume-integrated mass fluxes accumulated over time at the beginning of each outer (time) iteration, is shown in Figure 2. Notice there that the growth in mass conservation error is lower for the case where an “open” boundary condition is set for the outlet. However, for this relatively simple case the cumulative mass error is not too high in either case.

Finally, it can be concluded that for the purposes of the present work using either boundary conditions is relatively unimportant, from a stability point of view. However, it is important to remark that even for simple 2-D scenarios with high-quality grids and no pseudo-time stepping stability issues arise for “open” boundary conditions.

<sup>5</sup>Details on the settings are incidental to the discussion.

### 3 Verification and Validation: Hydraulic jump

*With four parameters I can fit an elephant,  
and with five I can make him wiggle his trunk.*

– John von Neumann (1948)

The previous chapters should form the foundation of what comes next: a set of numerical experiments geared towards the verification and validation of the postulates and algorithms previously discussed. Here, a quantitative and qualitative validation of the results obtained will be conducted using a grid refinement study on surrogate cases.

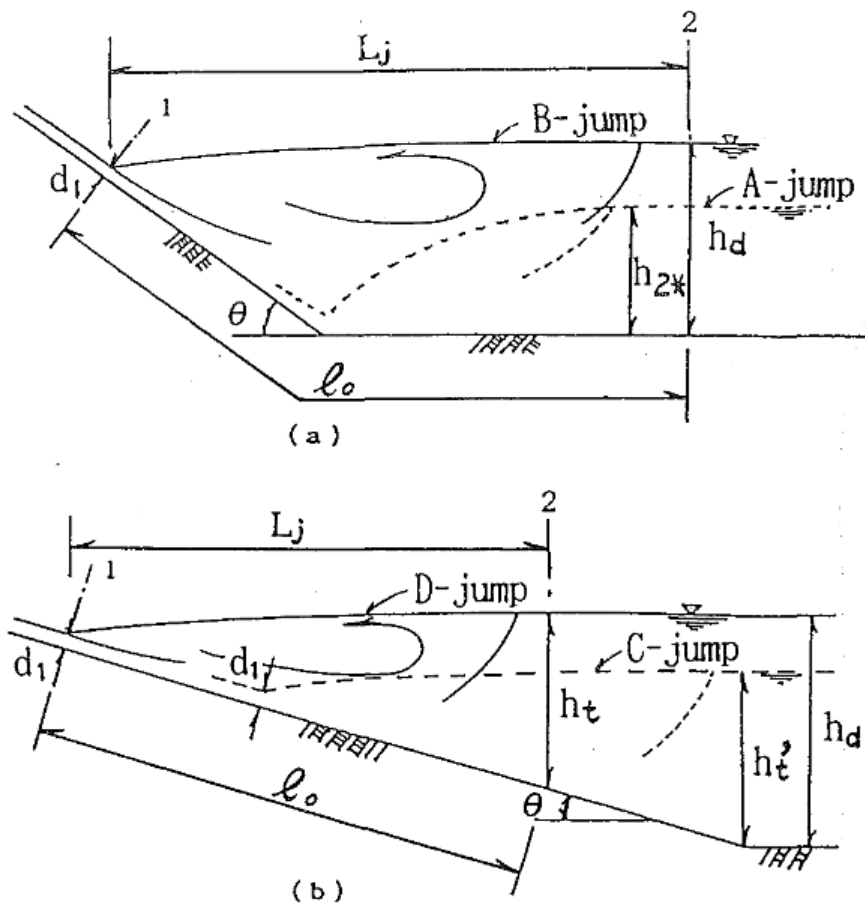


Figure 3 – Types of hydraulic jumps in sloped channel transitions as theorized by Ohtsu and Yasuda, 1991. Notice that the A-type jump corresponds to a CHJ.

Most importantly, this validation and the present report in general, concerns the study of hydraulic jumps in the stable regime and occurring on slope transitions (see Figure 3).

### 3.1 Previous grid-refinement studies: challenges and misconceptions

In general it is important to understand that one can only prove heuristically whether a flow is amenable for RAS: a feedback cycle between steady and unsteady features due to the large amalgam of scales provided by the Navier-Stokes equations makes it impossible to know, a-priori, whether RAS is suitable. In other words, possible stiffness in the solution<sup>6</sup> produced by so-called oscillations may sometimes be attributed to resolved unsteady features rather than to dispersive errors produced by the operators used therein.

One may, naïvely, assume that a grid refinement study is sufficient to reduce the uncertainties due to grid quality and linearization, and such would be true if it were not for the inherent unsteadiness present in hydraulic jumps. In the context of RAS it is difficult to discern between spurious and physical *oscillations*, that is, whether the lack of convergence in the solution's system residuals may be due to oscillations that correspond to *resolved* scales on the flow. Clearly, as one refines the grid the oscillations become more apparent and part of the "unsteady behaviour" (i.e. TKE, dissipation) that was once being modelled by the turbulence model becomes now *resolved* by the grid, but not accounted back by the model itself, producing instabilities. The turbulence model suggested herein attempts to account for these *oscillations* coming from disparate time-scales, at least partially.

Table 1 – Grid convergence history for different RAS models used in the study of so-called *classical* hydraulic jumps. For details on the study refer to Bayón *et al.*, 2019.

	$\Delta x$ (mm)	$p$ -	GCI %
STD. $k-\epsilon$	5.0	1.5	5.9
RNG. $k-\omega$	5.0	2.7	11.6
$k-\omega$ SST	5.0	2.1	4.5

In fact, some validation studies (Bayón *et al.*, 2019) related to RAS show rather disparate convergence history patterns for different turbulence models, as reproduced in Table 1. What's interesting in the aforementioned table is the *order of convergence*,  $p$ , which shows greater values than the theoretical maximum of 2 for PISO-based solvers in FOAM<sup>7</sup> for the  $k-\omega$  models. This disparity may confirm the hypothesis of the authors regarding the superiority of the STD  $k-\epsilon$  model, if one disregards the presence of unsteady, yet physical, space-time fluctuations present in hydraulic jumps. One may argue, however, that the supposed *goodness* exhibited by the STD  $k-\epsilon$  model may be due to its over-dissipative features suppressing the physical oscillations being resolved by PISO. It is well known that the STD  $k-\epsilon$  model tends to be over-dissipative in regions with strong adverse pressure gradients, and under-predict specific dissipation in regions where the flow present strong curvature (like in rollers). In any case, the authors fail to examine why such disparity occurs and what leads them to believe the STD  $k-\epsilon$  model is the preferred choice, beyond the simplistic reasoning based on monotonic<sup>8</sup> convergence of the solution towards values somewhat in agreement with literature formulae.

Given the aforementioned challenges, it becomes then difficult to assess whether the standard RAS turbulence models tested by Bayón *et al.*, 2019 are *stable* for VoF flows in general, or whether these are just unstable for the hydraulic jumps in questions. Thus, a grid convergence study will be devised in two steps: One where the stability of the proposed algorithms can be proven for flows that exhibit features present in hydraulic jumps but achieve a final steady state, and (2) where stability can be proven for cases involving unsteady hydraulic jumps, assuming RAS modelling is still valid for the scales being solved and some lenience in the turbulence scales. In the following sections, two grid convergence studies will be devised using two different flow archetypes.

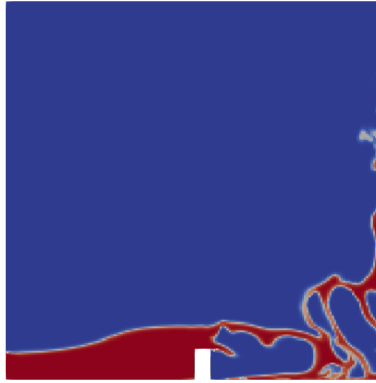
<sup>6</sup>Understood as difficulty of the linear solvers to reach convergence.

<sup>7</sup>Even that theoretical maximum is never achieved in practice, given the first-order-in-time nature of PISO.

<sup>8</sup>Although it clearly is not monotonic, by looking the GCI.

### 3.1.1 Grid Convergence Study: trivial archetype

The previous section delineated the reasons a convergence study, using the hydraulic jump as basis, may prove complex for analysing the *goodness* (stability, monotonicity) of a turbulence model. Remember that is difficult to distinguish physical, numerical, from spurious oscillations in physically unsteady cases, particularly as the grid becomes finer. However, this does not preclude the possibility of conducting a grid refinement study on a *simpler* archetype, that is, an archetype that exhibits features similar to those of the hydraulic jump but reaches a stationary, or trivial, solution as  $t \rightarrow \infty$ . The solution must only exhibit features common to the hydraulic jump in the transient phase, though.




---

Figure 4 – Dam break simulation at  $T = 0.5$  s.

---

A perfect candidate is the dam break case, given its simplicity and familiarity amongst FOAM users. The case geometry is taken from the standard tutorials of FOAM while the settings, turbulence model, and solver, are as described previously. However, the grid spacing is set to uniform and the initial spacing is  $\Delta x = 11.68$  mm.

The transient phase of the dam break case is shown in Figure 4, which exhibits wave-breaking and air-water entrainment, and as time passes the solution becomes fully stationary (quiescent liquid). At the end of the simulations, different metrics may be taken on the quasi-stationary solution and the order of convergence studied.

The L2-Norm of quantities representative of the different equations being solved, such as pressure or velocity for the predictor-corrector algorithm, and the residual viscosity for the turbulence models, represents a useful metric for the present analysis. The L1-Norm<sup>9</sup>, on the other hand, of the volume-fraction scalar is representative of both mass-conservation and convergence of the color equation.

As a reminder, the L2-Norm of a quantity  $v$  may be determined in the following way:

$$\|v\|_{L2} = \left( \int_{\Omega} v^2 d\Omega \right)^{1/2},$$

where  $\Omega$  is a domain in  $\mathbb{R}^n$ . Additionally, the order of convergence  $p$  for successively refined grids (labelled 1, 2, and 3) with a constant refinement ratio  $r$  may be determined in the following way:

$$p = \ln \left( \frac{f_3 - f_2}{f_2 - f_1} \right) / \ln r, \quad (19)$$

where  $f$  is some metric used to evaluate the order of convergence, in this case the L2-Norm.

The results for the grid convergence analysis using the dam break case on 3 successively refined orthonormal grids with  $r = 2$  are presented in Table 2. Based on the linearization practices suggested in Listings 2.1 for

---

<sup>9</sup>or volume integral

Table 2 – Grid convergence analysis for  $r = 2$  using the dam break case.

Grid Label	Mass-conservation ( $\alpha$ )	Momentum ( $\ \mathbf{u}\ _{L2} \times 10^{-5}$ )	Turbulence ( $\nu_t \times 10^{-6}$ )
1	0.0762817	14.4830	4.57505
2	0.0847463	10.1360	3.84557
3	0.106473	8.6851	2.21182
$p$	1.3599	1.5830	1.1700

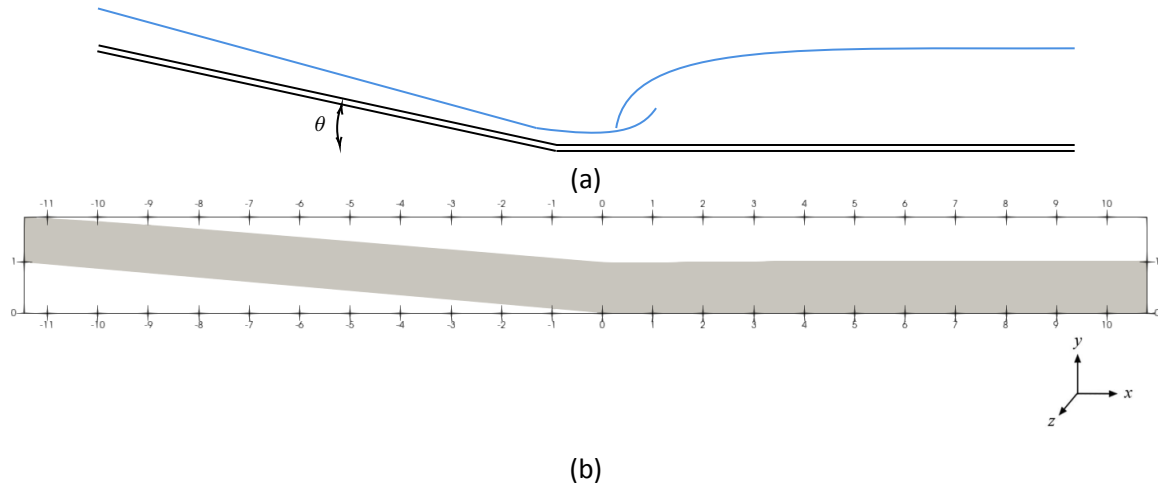


Figure 5 – Classic hydraulic jump downstream of a slope with angle  $\theta$ : (a) sketch of the problem, (b) numerical domain.

the different spatial and temporal operators, it seems only logical to obtain different convergence orders for the different equations being solved. Note that the assumed convergence order of the time operator is *locally* second-order, whereas for the gradient operator is *strictly* second-order accurate, and for the rest of the operators it lies in between.

The lowest convergence order is obtained for the turbulence model, which is expected, given the upwinded schemes therein used for the divergence operators plus the *deferred-correction* treatment of the non-linear coupling production terms present in Equations 8 and 9. On the other hand, the highest rate of convergence is obtained for the PISO algorithm, where the time operator and the deferred treatment of the non-linear convective term in PISO lower the convergence of the momentum.

### 3.1.2 Grid Convergence Study: second archetype

The previous section showed that the proposed algorithms converge monotonically for inherently *steady* solutions which, during the transient phase, exhibit features similar to those of a hydraulic jump. The next step is to test whether ensemble-averaged solutions from transient snapshots calculated for successively refined grids also converge monotonically. In this case, a classical hydraulic jump on a wide channel is proposed as an archetype for the grid convergence study.

Monotonic convergence of ensemble-averaged (U)RAS solutions present some challenges, particularly when the underlying flow is inherently unsteady. On one side, excessive mesh refinement may lead to the *over-resolution* of unsteady inertial features that may produce excessive dissipation on the turbulence model and produce the switch between different wall-model behaviour as the  $y^+$  approaches unity. On the other end, a too coarse grid may introduce also excessive dissipation via artificial viscosity and may not be able to represent important inertial features of the flow. In the particular case of a hydraulic jump one may want a grid fine enough to be able to accurately represent the incoming high-Froude supercritical flow, but yet coarse enough so to guarantee the wall models do not switch behaviour during the refinement stages or to avoid the first



off-wall centroid falling into the buffer zone  $11 < y^+ < 100$ . Furthermore, it is important also to avoid large cell aspect ratios when using VoF solvers as the compressive term in the color equation may tend to “stretch” the water body during splashing and wave breaking.

Table 3 – Grid convergence analysis for  $r = 2$  using the hydraulic jump case. A 4th refinement step is done, but not used for the calculation of  $p$ . Notice that the metrics for the 4th refinement are not monotonic anymore.

Grid Label	Mass-conservation ( $\alpha$ )	Momentum ( $\ \mathbf{u}\ _{L2}$ )	Turbulence ( $\nu_t \times 10^{-5}$ )
1	2.67634	2.13260	1.02503
2	2.77605	2.47026	1.20674
3	2.81602	2.59601	1.28919
4	2.88517	<u>2.46830</u>	0.41270
$p$	1.319	1.425	1.145

The mesh spacing was chosen to be uniform in all directions, but not equal, that is, an aspect ratio bigger than unity was set. In the direction parallel to gravity, the vertical mesh spacing for the coarsest grid was set to be  $\Delta y = 10$  mm assuming that the incoming supercritical flow is  $\mathbf{F} = 8$  and water depth is  $y = 60$  mm. An aspect ratio of 10 was chosen for the spanwise and streamwise directions. The viscosity of water was artificially reduced to  $1 \times 10^{-10}$  in order to guarantee the wall models to “stay” in the high-Reynolds regime as the mesh is refined. A sketch of the domain is shown in Figure 5, where the slope of the channel is set to  $\theta = \pi/36$ . The slope before the jump is needed in order to enforce a fully developed flow before the hydraulic jump in the flat channel.

Results of the grid convergence study are shown in Table 3, on three successively refined grids. Note that the order of convergence for the different *ensemble-averaged* quantities resemble those of the previous study where momentum ranked the highest order of convergence and the turbulence model ranked the lowest. The grid labelled “2” (first refinement) shows good quality metrics, not so different from the ones used for the fine grid (labelled “3”). The mesh spacings for case 2 will be used as basis for the rest of this work.

Non-monotonicity in the solution arises once the grid is refined for a fourth time, where the minimum grid dimension becomes  $\Delta y_{\text{very fine}} = 5/8$  mm and the maximum shear depth in the sloped channel is  $\overline{y^+} \approx 87$ . As explained before, many factors contribute to such behaviour: (1) over-resolution<sup>10</sup> of unsteady features, (2) mis-behaviour of wall-models, and (3) degradation of grid quality.

## 3.2 Validation using A-type (or classical) hydraulic jumps

The previous section dealt with *stability* and *convergence* of the code used within FH for the simulation of two-phase flows in general settings. There, it was shown that the present turbulence model and algorithms produce monotonic results as the grid becomes finer, within limits. However, the question of accuracy has not been addressed yet.

This section will then examine numerical results of classical hydraulic jumps after inclined slopes, or A-type jumps (Ohtsu and Yasuda, 1991), on a geometry as shown in Figure 5. Note that the present case allows for the verification of quantities *before and after* the hydraulic jump, based on one-dimensional descriptions, and permits a tighter control on the parameters defining the hydraulic jump’s behaviour.

The flow conditions and mesh constraints chosen for the present problem are shown in Table 4. Note that the channel is prismatic and rectangular in shape, and the mesh is refined close to the walls to a minimum of 5 mm, according to what was found in previous sections. In this case a *back-calculated* roughness for the channel is determined, which enforces the Froude Number described by assuming the supercritical flow in the slope is *uniform*, following Equation 21 (details given in the following section); such Froude number should

<sup>10</sup>Resolution of dissipative scales which, in principle, are being fully modelled by RAS

Table 4 – Case study conditions for the sloped channel.

	Value
$\mathbf{F}_1$	4.08
$q_{\text{inlet}}$	332 l/s/m
$\kappa$	1.0 mm
Channel Width	wide
$\rho_{H_2O}$	998.1 kg/m <sup>3</sup>
$\nu_{H_2O}$	$1.02 \times 10^{-6} \text{ m}^2/\text{s}$
$\Delta y$ (min)	5 mm
$\Delta y$ (max)	20 mm
$\theta$	$\pi/36$

guarantee a stable jump ( $\mathbf{F} = 4.85 > 4.5$ ). The slope of the channel is chosen to be steep enough to guarantee S3-type flow (steep), in a range where the basic relations of hydraulics are still valid. The flow at the domain's inlet is set uniform with direction parallel to the bed, and the water depth is set 20% higher than the uniform supercritical depth and let develop as it pours down the slope. It is expected that the flow develops *fully* before the hydraulic jump. The results herein showed correspond to those with an “open” boundary condition at the outlet. However, setting either a Dirichlet condition or an “open” boundary condition for velocities at the outlet shown no discernible difference in the results (see Figure 2); however, it is worth mentioning that the latter led to somewhat longer execution times.

### 3.2.1 Fully developed inflow: verification of the stresses

Here, one may derive simple (and exact) relations for the shear stress for the sloped channel and compare such relation with numerical calculations in order to validate the latter. It is clear that with the validations of the wall shear stresses one proves that: (1) the turbulence wall model behaves correctly for uniform flows, but also (2) that the flow is indeed fully developed before the jump.

As previously mentioned, an exact relation for the wall shear stresses given the wall roughness and the upstream, uniform, Froude number can be derived. This is possible because when the flow is uniform on a sloping channel, the overall wall stress between two sections MUST balance the longitudinal weight component of water contained between these sections at all times. The wall shear stress for a *wide* rectangular channel is then expressed in the following way:

$$\tau_{\text{wall}} = \gamma_{H_2O} y_n S_0, \quad (20)$$

where  $\gamma_{H_2O}$ ,  $y_n$ , and  $S_0$ , are the specific weight of water, normal depth, and channel's slope, respectively. By virtue of the Darcy-Weisbach definition, an exact relation between the friction coefficient  $f = f(\kappa, \mathbf{R})$  on a channel and its respective stress can be determined,

$$\tau_{\text{wall}} = \frac{\rho_{H_2O} f V^2}{8}, \quad (21)$$

and used to calculate, say, an appropriate wall roughness  $\kappa$  according to the desired upstream Froude number (i.e. water depth). Thus, repeated iterations of Eqn. 20, Eqn. 21, with an appropriate expression for  $f = f(\kappa, \mathbf{R})$ , may give the roughness of the upstream channel as function of the discharge and desired water depth. In fact, the Froude Number and corresponding roughness<sup>11</sup> presented in Table 4 were estimated that way.

Here, the assumption of low uniformity in the supercritical stretch of the channel flow must be verified in the numerical calculations along with the cross-section-integrated shear stress along the channel. To that end, a

<sup>11</sup>The Colebrook-White equation for  $f$  was used in this work.

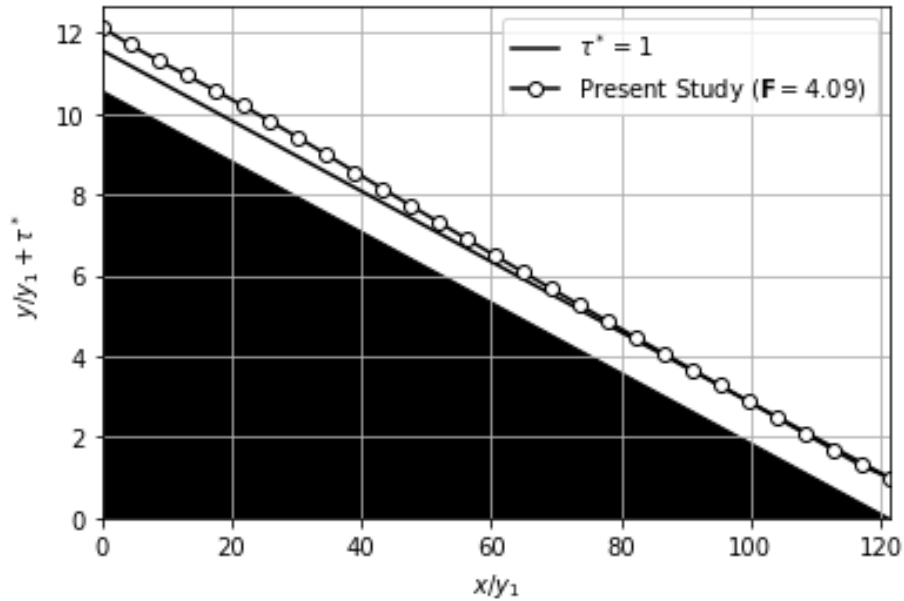


Figure 6 – Time-averaged 1-D profile of cross-section-integrated bottom shear stress for the sloped section of the channel, normalized using the hydraulic jump height  $h_j$ .

one-dimensional time-averaged profile of the shear stresses along the sloped channel is extracted from the simulations, as shown in Figure 6. There, the relation  $\tau^* = (\tau_{\text{wall}}/\tau_{\text{wall}}^{\text{CFD}})$  is used to compare the exact solution given by Equation 20 with the stress calculated by the simulations,  $\tau_{\text{wall}}^{\text{CFD}}$ . It is clear from the figure that the flow reaches uniformity at around  $x/h_j \approx 25$ , close to the toe of the slope. Since the hydraulic jump occurs *just after the toe* and flow decelerates as a consequence of the slope change then deviations from unity are expected just before the toe of the slope.

A verification of the velocity profiles against literature data at the point where the flow becomes uniform may offer further insight on whether the turbulence model and associated rough-wall models are working as expected. Figure 7 shows the velocity profile for the fully-developed flow in the supercritical region in the sloped channel. There, the law of the wall for rough surfaces according to Aupoix and Spalart, 2003 is used for comparison:

$$u^+ = \frac{1}{k} \left[ \log y^+ - \log \left( 1 - \frac{\kappa^+}{\exp(3.25k)} \right) \right] + 5.0,$$

where  $k \approx 0.41$ , and where the plus superscript denotes viscous normalization of the otherwise dimensional variables. The numerical results exhibited in the previous figure show a slope somewhat steeper than it is expected but the results are, generally speaking, in good agreement with the law of the wall. However, the effect of the lateral walls and flow confinement may be a contributing factor to the change in slope seen in the velocity profile as it has been shown to be the case for one-phase LES of flows in square ducts (Madabhushi and Vanka, 1991).

It is nonetheless important to mention that, unlike the present work, flow uniformity before the jump is rarely discussed in literature regarding the simulation of hydraulic jumps within RAS. The reason being that these studies only consider the flat section of the channel, where no exact relation can be derived for the wall shear stresses under flow uniformity arguments.

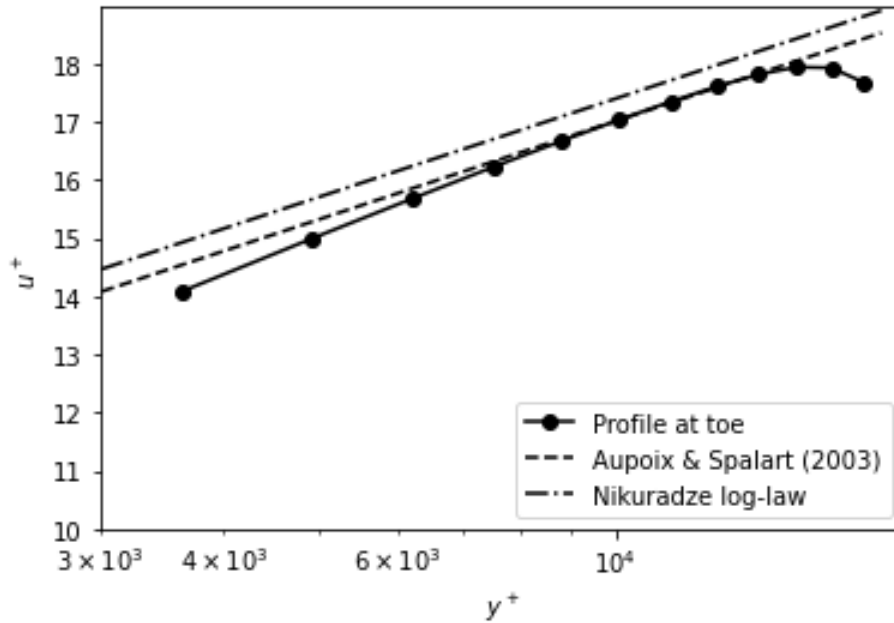


Figure 7 – Velocity profile of the fully developed supercritical flow in the sloped channel for the outer layer ( $R > 1000$ ), presented in viscous units.

### 3.2.2 Volume-of-Fluid verification: shape of the hydraulic jump

In previous sections a validation of the velocity field and shear stresses obtained in the supercritical section of the channel was performed, from the basis that the accurate representation of these fields against 1-D descriptors will validate the turbulence and wall model for its use in two-phase supercritical flows. There, indirectly, Equation 2 was also verified: the balance of stresses as presented in Equation 20 cannot yield correct results numerically if the weight of the fluid (i.e. water depth) is not accurately represented for an uniform flow. In fact, a fast verification of the water depth at  $x/y_1 \approx 80$  yields a Froude number equal to  $F_1 = 4.09$ , which is quite similar to what is assumed in Table 4.

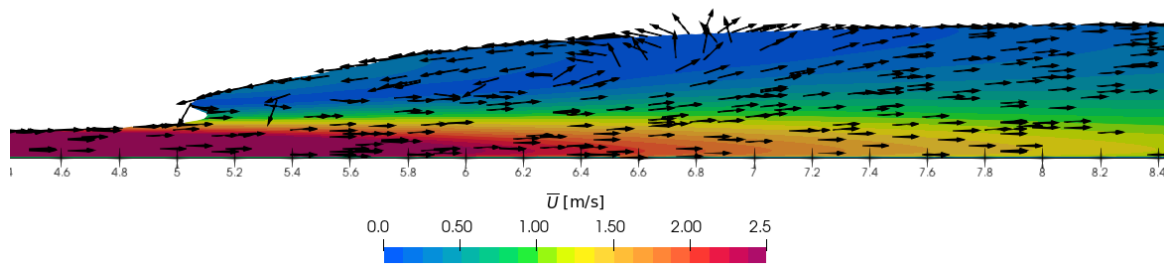


Figure 8 – Visual inspection of the hydraulic jump's roller length via surface flow patterns using the time-space averaged velocity field.

This section will follow the same logic for the validation of the color equation (Eqn. 2) but for the region comprising the hydraulic jump, that is, the section that begins at the toe of the jump until the end of the surface roller. The water surface profile in the aforementioned transect is depicted in Figure 9, where the horizontal and vertical scales are normalized using the *roller length*,  $L_r$ , and the hydraulic jump height,  $h_j$  (refer to Figure 19 for the notation). The length of the roller can be roughly estimated by inspecting Figure 8, which leads to a length of approximately  $L_r = 2.6 \text{ m}$  measured from the toe of the jump ( $x \approx 5.0 \text{ m}$ ) until where all the flow vectors more or less follow the main path of the flow ( $x \approx 7.6 \text{ m}$ ). Note that the use of the following

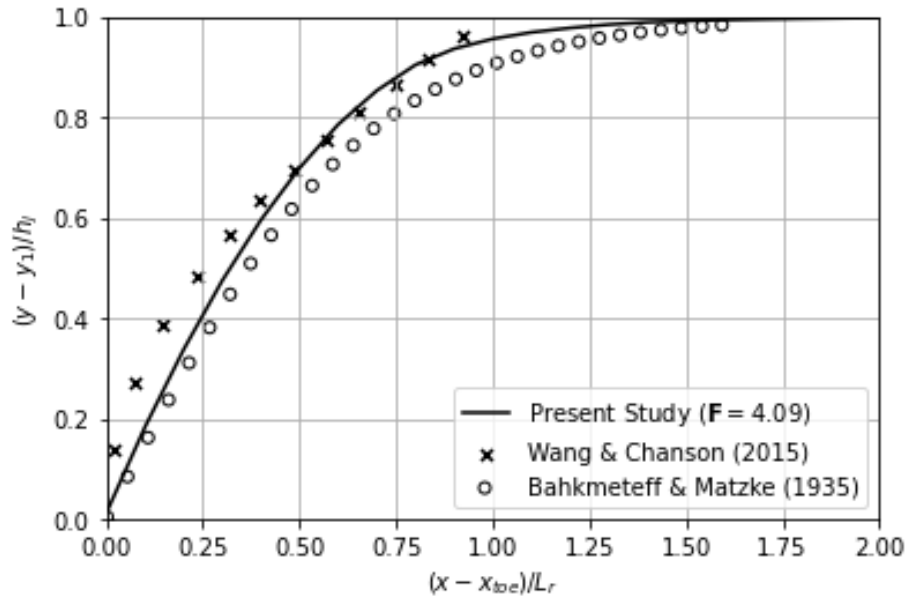


Figure 9 – Normalized shape of the hydraulic jump.

formula,

$$L_r = 220y_1 \arctan \frac{F_1 - 1}{22}, \quad (22)$$

for the present case gives a theoretical  $L_r \approx 2.70$  m, which is not so different from the aforementioned measurement.

The results obtained from the simulations match quite closely with the experimental studies of Bakhmeteff and Matzke, 1936. More recent studies accounting for bubble dynamics (Wang and Chanson, 2016) show a steeper increase in the water surface profile compared to the present study.

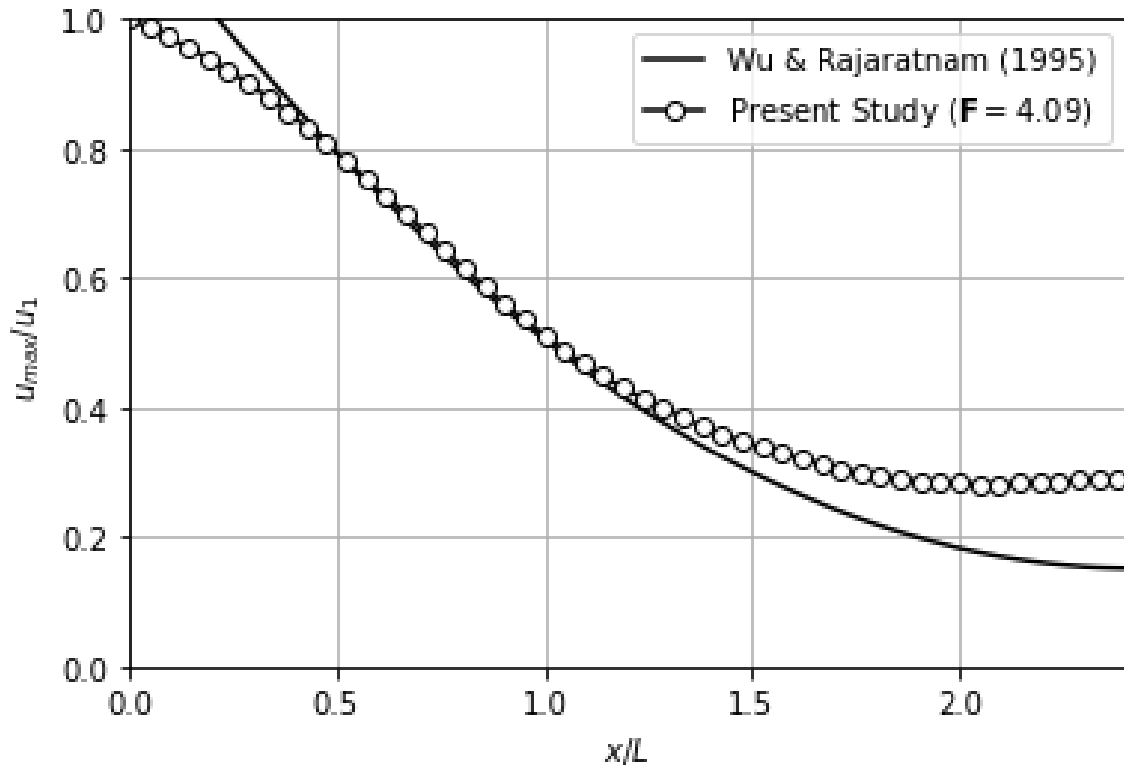
### 3.2.3 Dynamics of the flow within the hydraulic jump

The internal flow and turbulence characteristics of several types of hydraulic jumps have been studied for decades now (Bakhmeteff and Matzke, 1936; Hornung *et al.*, 1995; McCorquodale and Khalifa, 1983; Ohtsu and Yasuda, 1991; Peterka, 1964; Rouse *et al.*, 1959). In particular, the work of McCorquodale and Khalifa, 1983 and the classical studies of Rajaratnam and Subramanya, 1968 can be used to validate the velocity fields and its decay along a hydraulic jump, in a RAS sense.

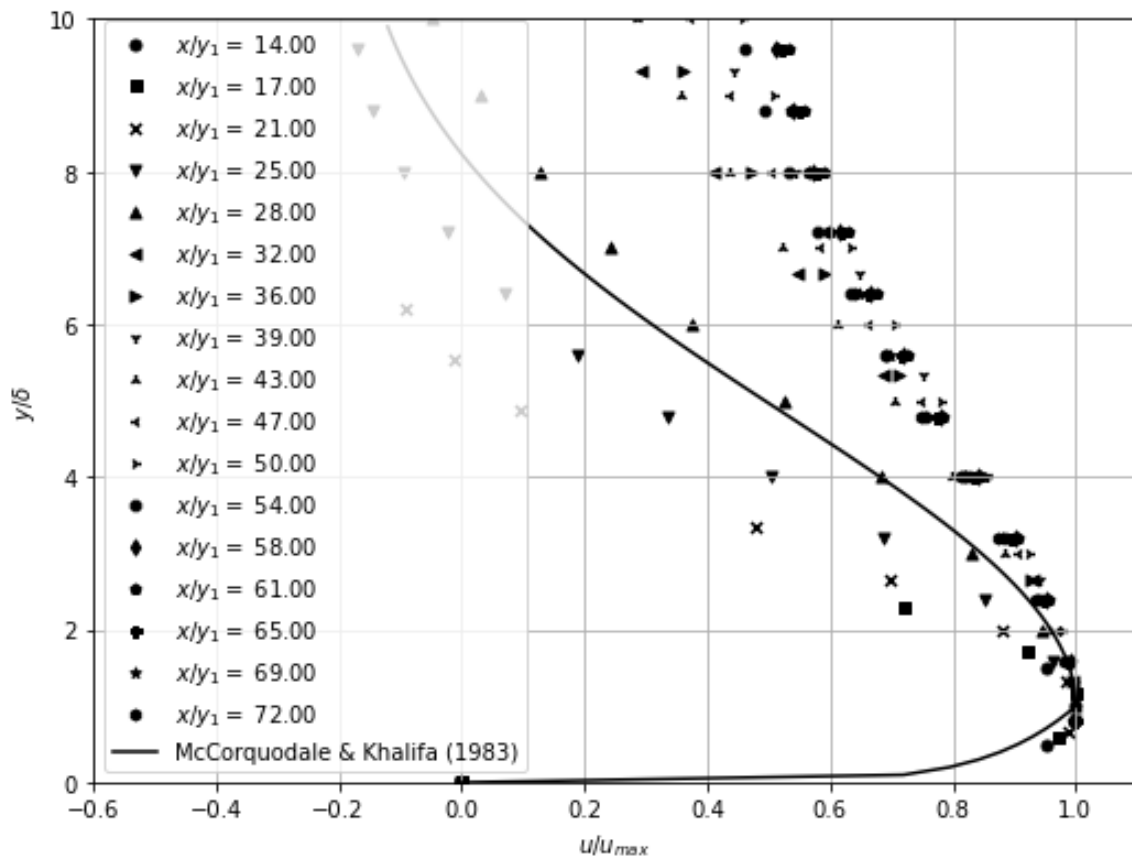
All the information regarding the internal flow dynamics of a hydraulic jump is condensed in Figure 10. The flow jet that forms underneath the surface roller in a hydraulic jump shares similarities with a classical non-buoyant jet flow (Rajaratnam and Subramanya, 1968; Wu and Rajaratnam, 1995); one may then express the maximum velocity decay in the following way:

$$\frac{U_{\max}}{u_1} = 1.173 - 0.843 \frac{x}{L} + 0.174 \left( \frac{x}{L} \right)^2,$$

where  $u_1$  is the mean velocity of the incoming supercritical flow, and  $L$  is the length where the maximum velocity reduces to half of  $u_1$ . It is clear that the aforementioned decay is modulated by the action of the surface roller, that is, an accurate modelling of the physics of the roller should lead also to a good prediction of the velocity decay. It should be noted then that the results in Figure 10-a indicate a good agreement between the decay for wall-jets and the predicted decay for A-type, or classical, hydraulic jumps. This, indirectly, also



(a)



(b)

Figure 10 – Internal flow characteristics of the A-type hydraulic jump for  $R_\tau \approx 17000$  and  $F = 4.68$ . (a) Maximum velocity decay along the axis of the jump, and (b) vertical profiles of velocity at different locations along the axis.

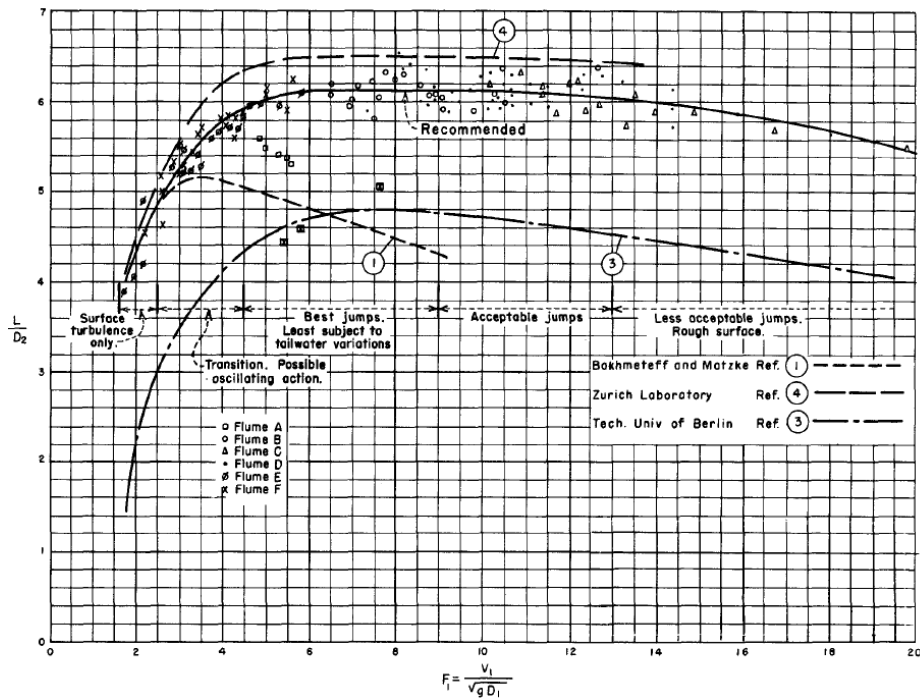


Figure 11 – Various experiments relating the roller length to the Froude number, conducted by various research groups (Peterka, 1964)

indicates that the algorithms herein proposed are satisfactory for the resolution of the surface roller within the context of RAS.

Moreover, the vertical profiles of velocity within the jump show fair agreement with the model of McCorquodale and Khalifa, 1983 in the region comprising the core of the roller ( $14 < x/y_1 < 32$ ). In general, the profiles match quite good with respect to Equation 13 for  $y/\delta < 1$ , but then some of the profiles outside of the core of the roller tend to have larger discrepancies from Equation 14. However, the overall trend of the wall-jet and surface recirculation are present on every single profile, discarding any spurious behaviour that may arise due to over-dissipation or incorrect simulation setup<sup>12</sup>. It is important to mention that other studies relating both numerical and experimental work have shown similar trends and discrepancies with respect to otherwise self-similar velocity profiles (Jesudhas *et al.*, 2018; Macián-Pérez *et al.*, 2020; Mortazavi *et al.*, 2014; Wang and Chanson, 2016). In fact, the DNS results presented in Figure 24 show non-similarity of the profiles for oscillating jumps.

### 3.2.4 How validate the surface roller length, $L_r$ ?

The exact definition of hydraulic jump's length, or roller length, was a subject of debate for quite some time (Peterka, 1964) and still is. Even in the case where the same scaling laws and parameters are used, different (reputable) research groups have come up with quite different results for the determination of the surface roller length, as it can be seen in Figure 11. Clearly, in engineering design one may strive to work with the most conservative of results when given various options hence the nature of the suggestion ("Recommended" line) put therein. The reasons for such differences lie both in the way how the data is scaled (with the sequent depth, instead of the more natural antecedent depth) and how the boundary of the roller is defined during visual inspection.

In this work, and numerical experiments in general, one can opt for a mathematical approach for the estimation of  $L_r$  by defining precisely where the shear region between the surface roller and the wall-jet lies. In previous

<sup>12</sup>Behaviour such as bottom recirculations due to flow separation, and such.



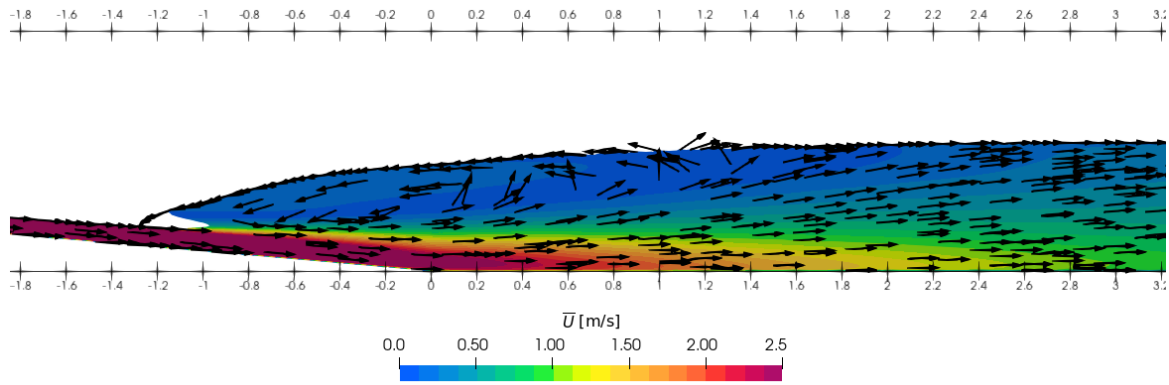


Figure 12 – Surface flow patterns for a B-type jump.

chapters by defining the so-called *von Karman Length*,  $L_{vk}$ , in a way suitable for the modelling of hydraulic jumps, a means of educing sheared region was also implied. In general, one may assume that  $1/L_{vk}(U) = 0$  represents the boundary between the roller and the wall-jet, as expressed in Equation 17. This metric, although mathematically sound, is quite complex to verify in engineering practice, and to measure or educe in experimental settings, thus it serves no use for the purposes of measuring  $L_r$ . Instead, the Author followed an approach similar to that used by several researchers in the experimental camp: visual inspection of flow streamlines.

However, by revisiting some of the already presented results one may notice that by accurately representing the water surface profile of the hydraulic jump using  $L_r$  as scaling factor it also implies that  $L_r$  itself is accurately defined in view of both the experimental and numerical values already shown in Figure 9.

### 3.3 Validation using B-type hydraulic jumps

Here, a validation similar to the one conducted in the previous section will be done. The difference here lies in the location of the hydraulic jump's roller: referring to Figure 5 it will be assumed that the roller region is partly on the slope, that is, further upstream from the previous scenario (A-type).

More specifically, a simulation was set-up using similar parameters described in Table 4, except for the downstream water level where 0.65 cm was set in order to produce a B-Type jump. Note that the supercritical flow on the slope may not be fully developed when it plunges the downstream pool. The present scenario is interesting for the following reasons: (1) the flow deceleration seen towards the toe of the slope will occur within the wall-jet in this case which may enhance the roller and affect the maximum velocities inside the jet, (2) as a consequence, the roller region will be enhanced, and (3) the effects of a non-fully developed incoming flow can be analysed.

In previous chapters, it was mentioned that flow decelerations may produce flow separation, even in hydraulic jumps given some conditions. There it was shown that flow separation in hydraulic jumps was more likely to happen in weak (or oscillatory), or drowned, jumps where decelerations are important. On the other hand, although sources of flow decelerations other than the roller exist for B-type jumps, there is no record of flow separation in the experimental studies revised in the present work (Ohtsu and Yasuda, 1991). Note that in the aforementioned study the experiments were conducted for stable jumps. Therefore a physically accurate CFD code should not exhibit secondary rollers (due to flow separation) at least for stable jumps ( $\mathbf{F} > 4.5$ ).

A first inspection of the flow patterns obtained for the present simulation indicates no spurious flow features or separation of any kind, as depicted in Figure 12. The supercritical flow upstream reaches a minimum depth equivalent to  $\mathbf{F} = 4.16$ , and the length of the roller may be estimated to be  $L_r = 2.2$  m.



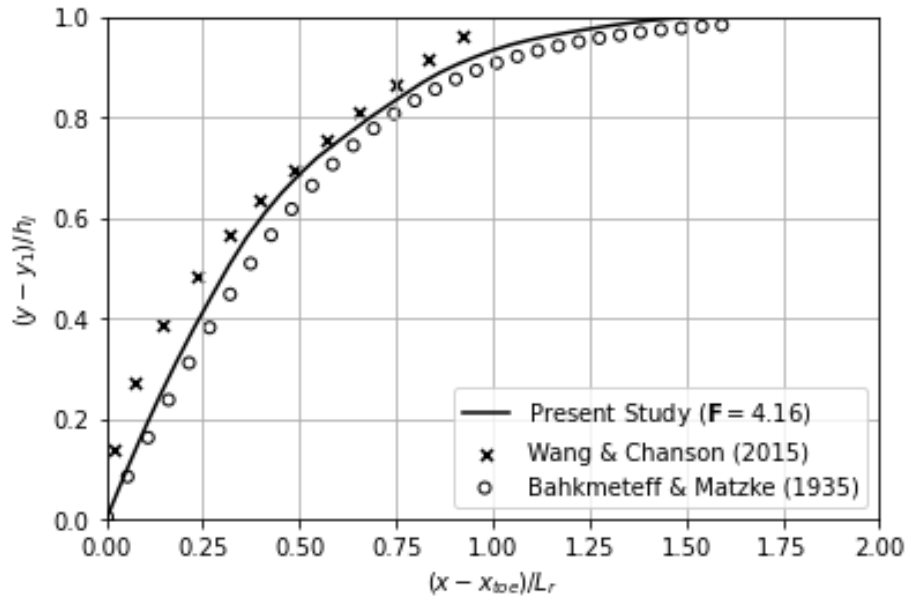


Figure 13 – Normalized shape of the B-Type hydraulic jump.

### 3.3.1 Shape of the B-type hydraulic jump

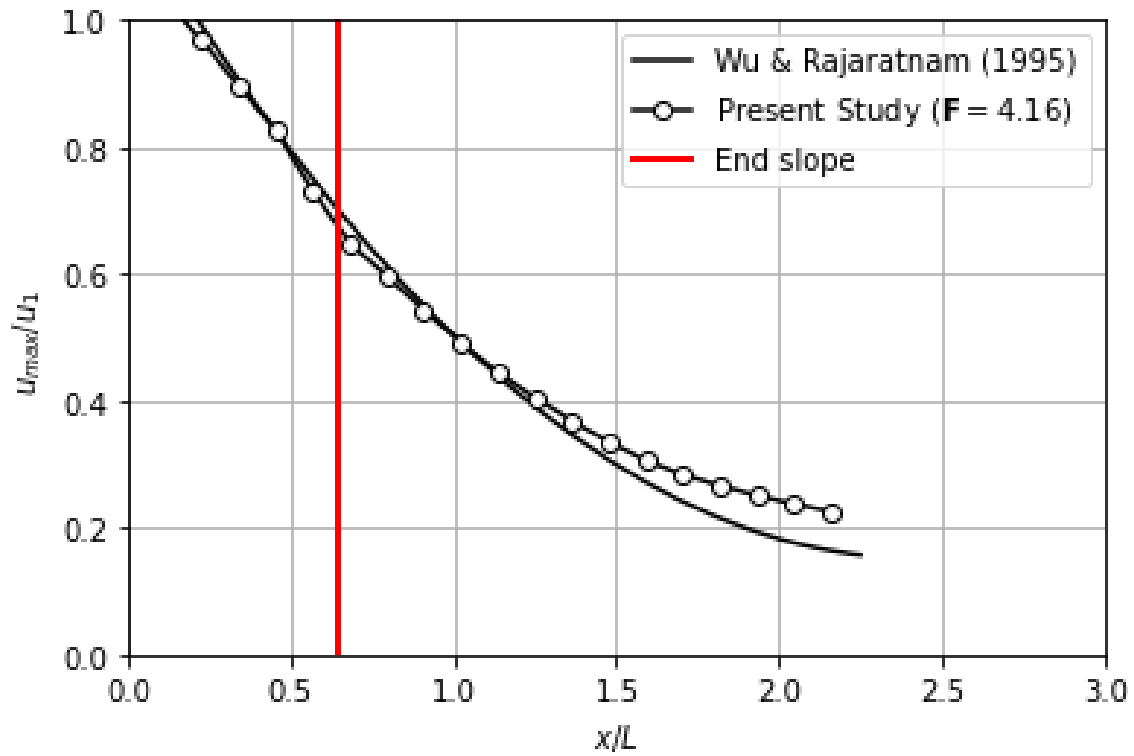
As mentioned earlier, the present simulation has a Froude number somewhat less than the simulation of the A-type jump discussed in the previous section. However, the shape of the hydraulic jump depicted in Figure 13 matches well with recent experiments conducted for similar Froude numbers (Wang and Chanson, 2016).

Clearly, the normalization of the hydraulic jump's profile is modulated by  $L_r$ . Note that the use of Equation 22 gives a  $L_r \approx 1.50$  m which shows that the length of the roller for B-Type jumps becomes larger compared to classical jumps. Previous studies (Ohtsu and Yasuda, 1991) have suggested B-Type jumps may have somewhat longer roller regions compared to classical hydraulic jumps. This follows from the fact that the flow jet beneath the roller *accelerates* downstream of the toe, producing a larger sheared region as a consequence.

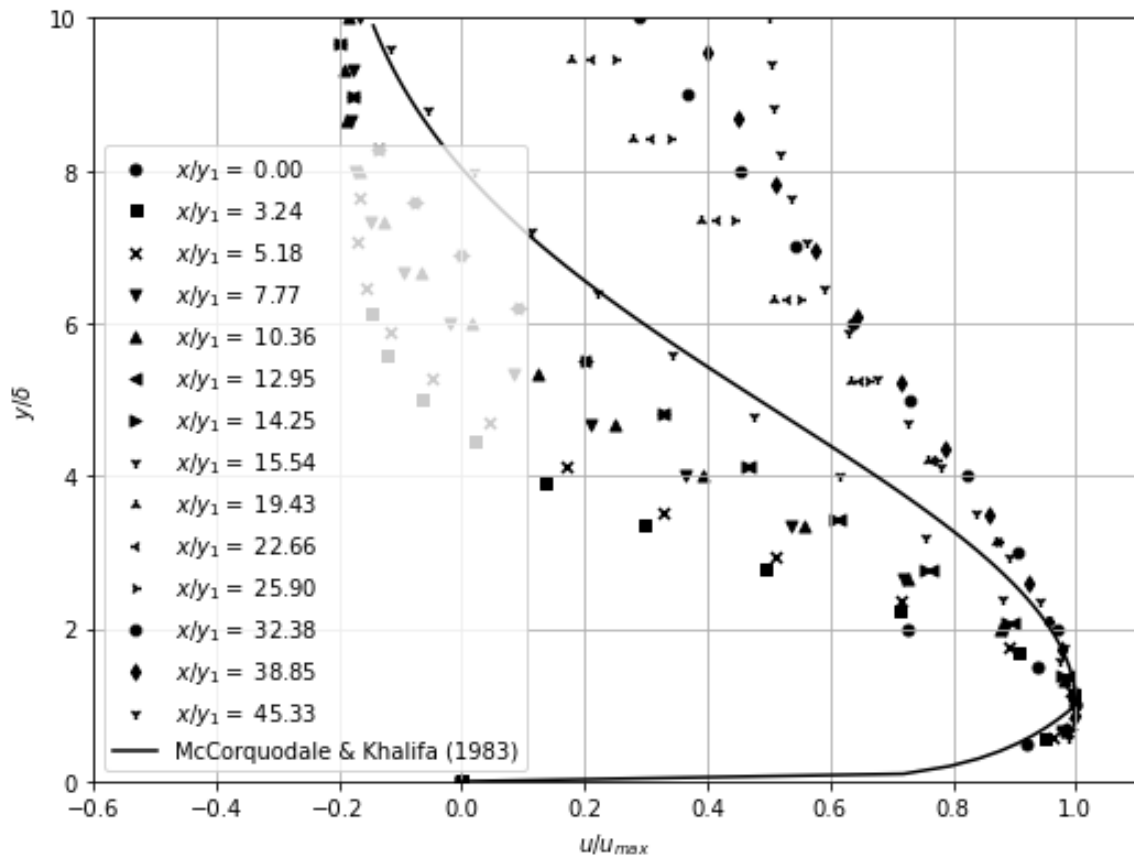
### 3.3.2 Internal flow mechanism of the B-Type jump

As done in previous section, an analysis of the internal flow features of the B-Type jump is conducted and presented in Figure 14-a and Figure 14-b. The former shows the velocity decay for the present case which, when compared to the results for the A-Type jump, show a stronger decay as one moves downstream in the Figure. It was mentioned previously that larger accelerations in the jet flow downstream of the toe of the slope may produce longer rollers which, given their increased energy, produce larger dissipation in the shear region shared with the jet underneath conducting to larger decay. Note that larger differences in velocity decay occur *after* the toe of the slope. Such assertion is also made by Ohtsu and Yasuda, 1991 and confirmed with the experiments conducted therein.

The velocity profiles within the hydraulic jump indicate a stronger roller region for the first  $x/y_1 \approx 10$  units, as seen in Figure 14-b. These profiles approach asymptotically the theoretical profiles of (McCorquodale and Khalifa, 1983) as  $y/\delta \rightarrow \infty$  and exhibit stronger gradients in the outer region  $y/\delta > 2$  giving indication that the coefficient modulating the slope in Equation 14; however, the velocity profiles change quite sharply for  $x/y_1 > 13$ , showing weaker gradients in the outer region. Such assertion goes hand-in-hand with the analysis presented previously about the velocity decay: enhanced dissipation after the toe of the slope produce a larger decay of the velocities. Finally, in none of the profiles spurious separation or recirculation are present in the inner region of the velocity profile.

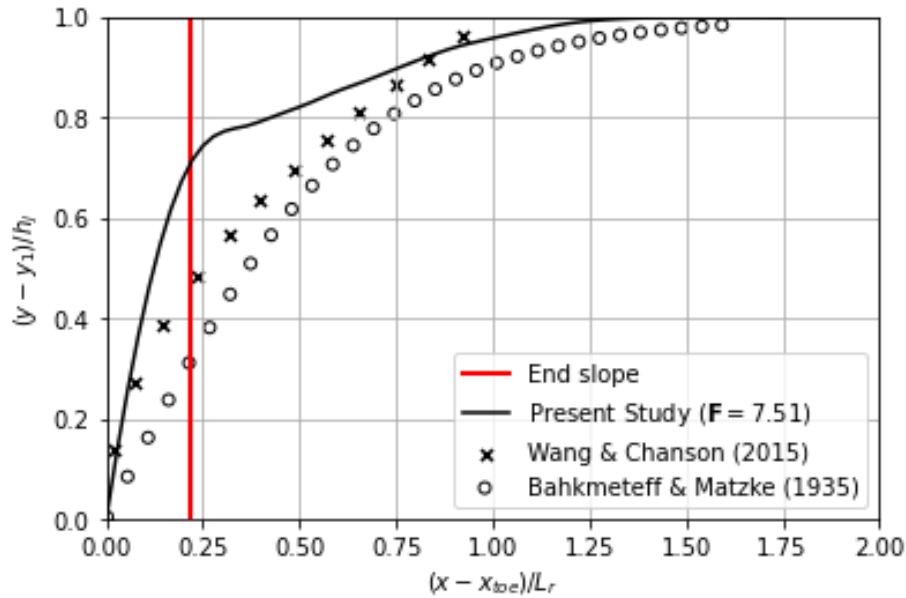


(a)

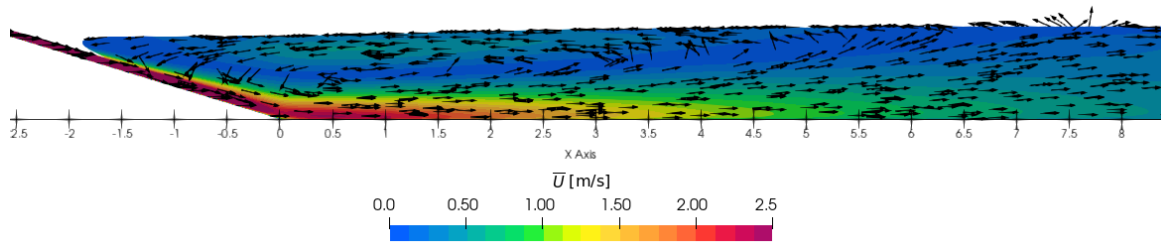


(b)

Figure 14 – Internal flow characteristics of the B-Type hydraulic jump for  $R_\tau \approx 16500$  and  $F = 4.68$ . (a) Maximum velocity decay along the axis of the jump, and (b) vertical profiles of velocity at different locations along the axis.



(b)



(b)

Figure 15 – (a) Normalized shape of the hydraulic jump and (b) Surface streamlines for the B-type jump in a steep slope.

### 3.4 Further insights using B-type hydraulic jumps on steep slopes

The previous sections have successfully shown the validity of the present turbulence model and numerical algorithms for the solution of two-phase flows for the study of different types of hydraulic jumps on flat and *mild* slopes. Here the numerical simulation of a B-Type hydraulic jump as described in Table 4 is conducted, with the only difference that the slope in the oncoming channel is increased to  $\theta = 17^\circ$ . Note that the Froude number just before the hydraulic jump increases sharply in this case,  $F = 7.51$ , due to the abrupt change of slope.

By increasing the slope of the channel to  $\theta = 17^\circ$ , some of the basic assumptions in classical hydraulics start to break down: balance of momenta along the axis of the channel must consider the weight of the fluid and corrections need to be made to the kinetic and potential energy terms in the Bernoulli equation. Even with such improvements, local accelerations product of slope changes are critical yet unresolved in unidimensional hydraulics. Experiments conducted by Ohtsu and Yasuda, 1991 indicate the existence of such sharp accelerations exactly at the toe of a steep slope with a flat channel.

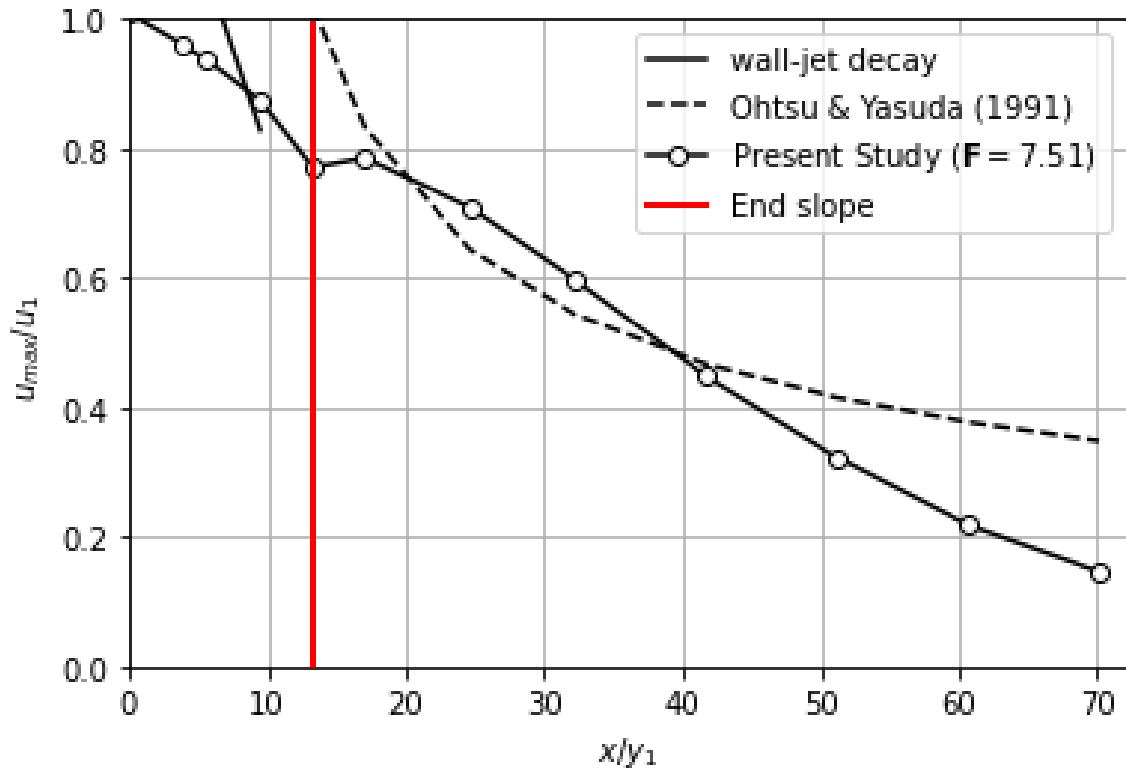
An example of such differences is in the shape of the hydraulic jump's profile before and after the toe of the slope as depicted in Figure 15-a, concomitant with the previous simulations. There, the length of the hydraulic jump is measured from the surface streamlines shown in Figure 15-b, which gives  $L_r = 3.6$  m. Note that Equation 22 reports a significantly lower value for the length of the roller ( $L_r \approx 2.0$  m). A change in the character of the flow is noticeable in the free surface profile, due to the substantial size of the roller. This variation must then be reflected in the internal flow behaviour in the hydraulic jump itself, that is, the increase

of the size of the roller (which drives the hydraulic dissipation within the hydraulic jump) must be consequence of internal accelerations that must be dissipated.

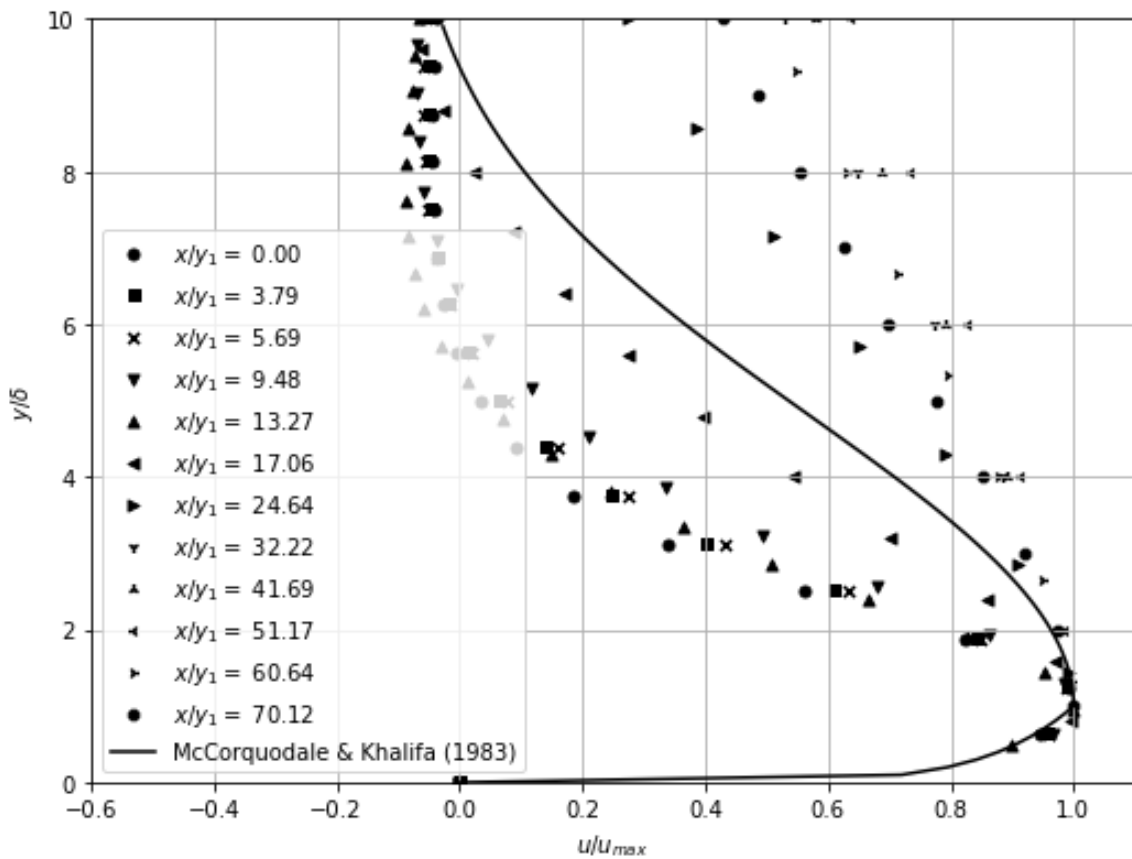
### 3.4.1 Internal flow character of the B-Type jump in steep slopes

Variations of the free-surface profile with experimental data were attributed to local accelerations that occur in the change of slope present in the geometry herein studied. As previously mentioned in other studies (Ohtsu and Yasuda, 1991) the so-called hydraulic dissipation, expressed in the velocity decay profiles shown in Figure 16-a, show a different character before and after the toe of the slope for B-Type jumps in sloped channels. Note in the figure that a jump in the velocity is present exactly where the toe of the slope is located, indicating that: (1) velocity decay behaves similarly to B-Type jumps in *mild* slopes, and (2) the sudden acceleration enhances the surface roller and produces a larger slope of velocity decay downstream of the toe.

The velocity profiles depicted in Figure 16-b also indicate a stronger shear region as most of the profiles for  $x/y_1 < 20$  become asymptotic to the abscissa for  $y/\delta > 6$ . However, for  $x/y_1 > 20$  the velocity profiles in the outer layer tend to approach the relative maximum velocity  $u/u_{\max}$  faster, compared to previously depicted results.



(a)



(b)

Figure 16 – Internal flow characteristics of the B-Type hydraulic jump for  $F = 7.51$ . (a) Maximum velocity decay along the axis of the jump, and (b) vertical profiles of velocity at different locations along the axis.

## 4 Discussion

The present work deals with the validation and verification of proposed turbulence models and simplifications of the governing equations of fluid flows according to the requirements of hydraulicians. The chosen archetype for the present campaign is the hydraulic jump, focusing on two scenarios: (1) a classical hydraulic jump on a flat bed, and (2) a B-Type hydraulic jump on a sloped channel. The first scenario is for which most of experimental and numerical studies have been dedicated to in the field of hydraulics, hence there is plenty of literature that serves the purposes of the present study. The second scenario is chosen because of its *dissipative* properties: of all types of hydraulic jumps, B-Type jumps are preferred because these produce the maximum velocity decay (or so-called dissipation, as intended by hydraulicians) for the same incoming Froude number.

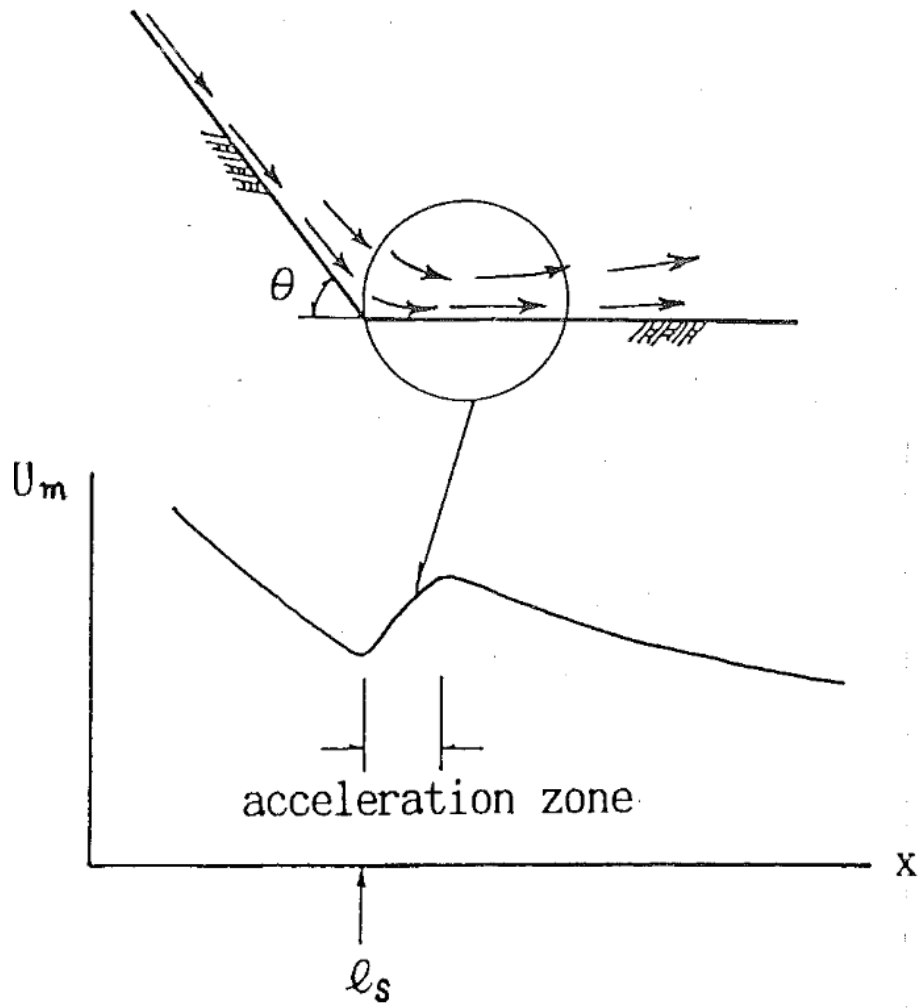
The nature of the surface roller and dissipation therein for B-Type jumps is function of the slope of the incoming channel. The results pertaining steep slopes reproduce what has been hypothesized and studied in previous works regarding the character of hydraulic dissipation (or velocity decay) within B-Type jumps in steep slopes, as sketched in Figure 17, that is, the change in character in the velocity decay before and after the toe of the slope. Unfortunately, there is not too much experimental literature about the internal flow structure of B-Type jumps in steep channels, except for the literature used in this work.

The numerical results herein presented show overall agreement with selected literature data, for stable hydraulic jumps. Spurious secondary currents and flow separation often seen in other CFD results are not present, and the solutions exhibit no influence from boundary conditions or of the simplifications conducted to the governing equations. Furthermore, the present verification shows that the proposed turbulence model is robust and gives satisfactory results, as well as the code itself.

Although not studied in the present numerical campaigns, the onset of separation cannot be considered always as *spurious* when seen in numerical simulations of hydraulic jumps. Different numerical studies and one-dimensional analysis under the lens of classical mechanics offer insight about the feasibility of separation under some *specific* circumstances, regarding hydraulic jumps. It was noted that the onset of flow separation is more likely in, say, drowned jumps, and oscillatory-to-weak jumps.

### 4.1 Future work

Given the satisfactory results obtained from the methodologies implemented herein, the next step is to further focus on numerical campaigns aimed into resolving features for weak-to-oscillatory jumps, and of stable jumps in sloped channels. Special emphasis on the location of the toe of the jump and of its length will be given, and comparisons will be made with literature data and experiments.



---

Figure 17 – Acceleration zone as theorized by Ohtsu and Yasuda, 1991.

---

# A1 Theoretical Considerations

(...) various aspects of the hydraulic jump, long subject to conjecture or misunderstanding, are thereby clarified.

– Hunter Rouse (1959)

This chapter will be devoted to discuss some generalities about hydraulic jumps, within the context of computational mechanics, physics, and engineering. The attempt here is to bring to the discussion the non-similar behaviour of hydraulic jumps, including flow separation, which, to some degree, is unbeknownst to some engineering practitioners. More precisely this chapter will attempt to find a common ground on why separation may occur in hydraulic jumps on certain circumstances, and for that it is necessary to re-visit the problem using *first principles* and high-resolution data (DNS or Experimental Fluid Dynamics (EFD)) produced elsewhere.

## A1.1 Theory, research, and practice of hydraulic jumps

A substantial amount of peer-reviewed articles have been (and continue to be) published on the subject of hydraulic jumps using CFD<sup>13</sup>. Said articles range from fundamental physics of hydraulic jumps (Jesudhas *et al.*, 2018; Mortazavi *et al.*, 2014; Witt *et al.*, 2018), verification and validation of CFD codes (Macián-Pérez *et al.*, 2020; Mukha *et al.*, 2020), to engineering applications under the context of eco-hydraulics. However, the fundamental physics of hydraulic jumps are well known since the 1960's (Rouse *et al.*, 1959). For the purposes of this report, just some salient results from previous research will be mentioned and some basic theory revisited.

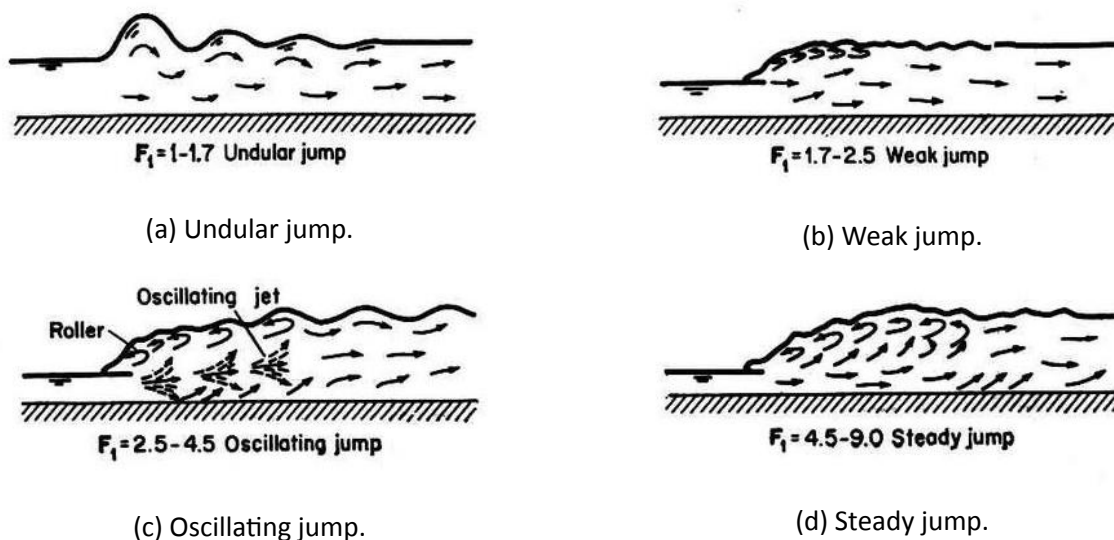


Figure 18 – Hydraulic jump classification according to the Froude number.

The most important aspect of hydraulic jumps is its *character*, or so-called type, according to the Froude number of the upstream flow, as shown in Figure 18. Up to date, a large body of literature has been devoted

<sup>13</sup>A simple *Google Scholar* search of the keywords 'hydraulic jump' and 'CFD' suggests a total of 11200 articles in the last 10 years



to the study of hydraulic jumps focusing on its features like energy dissipation, roller length, velocity field, and more recently aeration and bulking<sup>14</sup>, across all types, dealing with varying degrees of challenges. On the other hand, note that most of the literature regarding DNS/LES of hydraulic jumps involves oscillating and weak hydraulic jumps given the high computational demand required to accurately resolve the jump's features at higher Froude numbers. Thus, steady hydraulic jumps are only currently being studied via *Detached Eddy Simulations* (DES), and for jumps with higher incoming Froude numbers the research focus is on the accurate modelling of flow *bulking* and air entrainment via population models and the sub-grid scale modelling of bubble coalescence/breakup and turbulence therein. The present review will not focus on the latter line of research.

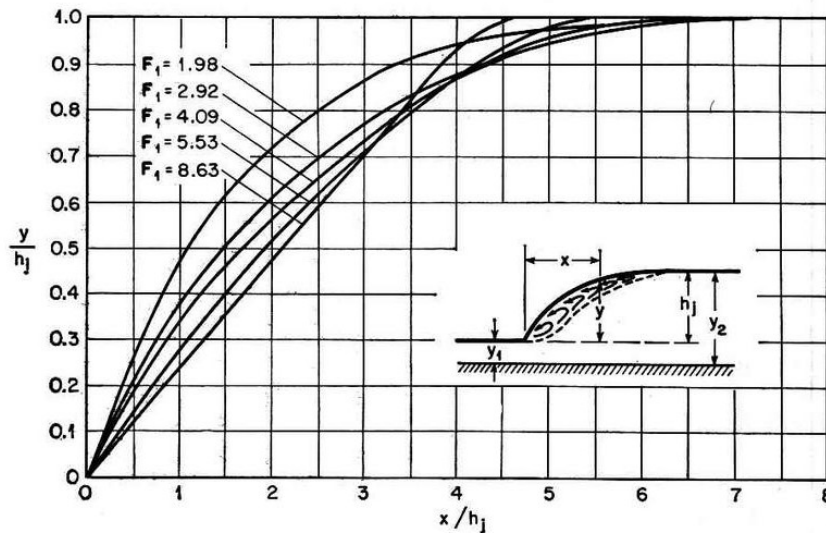


Figure 19 – Dimensionless surface profiles of hydraulic jumps in horizontal channels, taken from Peterka, 1964. Experiments were conducted originally by Rajaratnam and Subramanya, 1968.

In engineering practice all types of hydraulic jumps are assumed *self-similar*, that is, all families of hydraulic jump types collapse into a single representation which scale with the Froude Number. For detailed studies using high-resolution PTV or simulations, this is not the case (Wang and Chanson, 2016): (1) flow patterns, such as the surface roller or turbulence kinetic energy, are not self-similar across hydraulic jump types, and (2) air-water flow characteristics, such as air entrainment or jump length, cannot be correctly quantified at scale. This can be inferred by simply observing the non-dimensional jump profiles of Rajaratnam and Subramanya, 1968, shown in Figure 19, which do not collapse onto a single profile under varying Froude numbers.

On the other hand, the aforementioned assumption, although apparently incorrect, proves useful for the study of hydraulic jumps by means of two dimensional mass, momentum, and energy conservation under the assumption of irrotationality (Bakhmeteff and Matzke, 1936). A graphical representation of the characteristic equations used for the design of structures using hydraulic jumps (e.g. Stilling basins) in classical hydraulics is shown in Figure 20. These curves are prepared for the specific energy ( $E$ ), the water heights before and after the hydraulic jump ( $y_1$  and  $y_2$ ), for different upstream Froude numbers ( $F_1$ ), based on the generalized Bernoulli equation<sup>15</sup>. Notice that self-similarity from these equations cannot be assessed since for their derivation, it is assumed that the hydraulic jump represents a *discontinuity* in energy, and therefore, in the water surface profiles.

However the fact that one dimensional variations of energy and derived quantities thereof cannot be proven (or disproven) self-similar for a hydraulic jump, this doesn't imply that self-similarity can be disproven to more complete descriptions based on the governing equations of fluid flow. In other words, self-similarity in energy

<sup>14</sup>*Bulking* is the process whereby a supercritical flow on a hydraulically steep channel undergoes the formation of an air-water mix boundary layer starting from the free surface down to the bottom of the channel, increasing the depth of the flow.

<sup>15</sup>Local, considers entropy and heat losses.

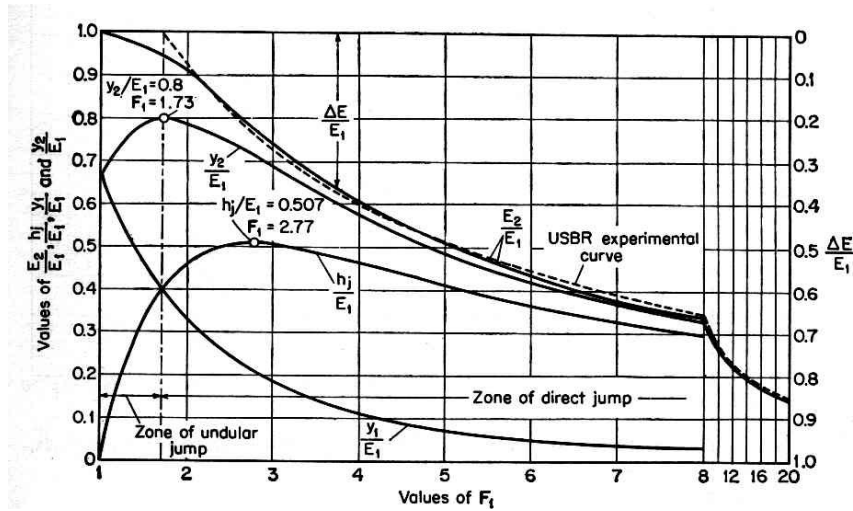


Figure 20 – Characteristic curves of hydraulic jumps in horizontal rectangular channels (Peterka, 1964). The sub-indices 1 and 2 refer to locations upstream and downstream from the jump, respectively.

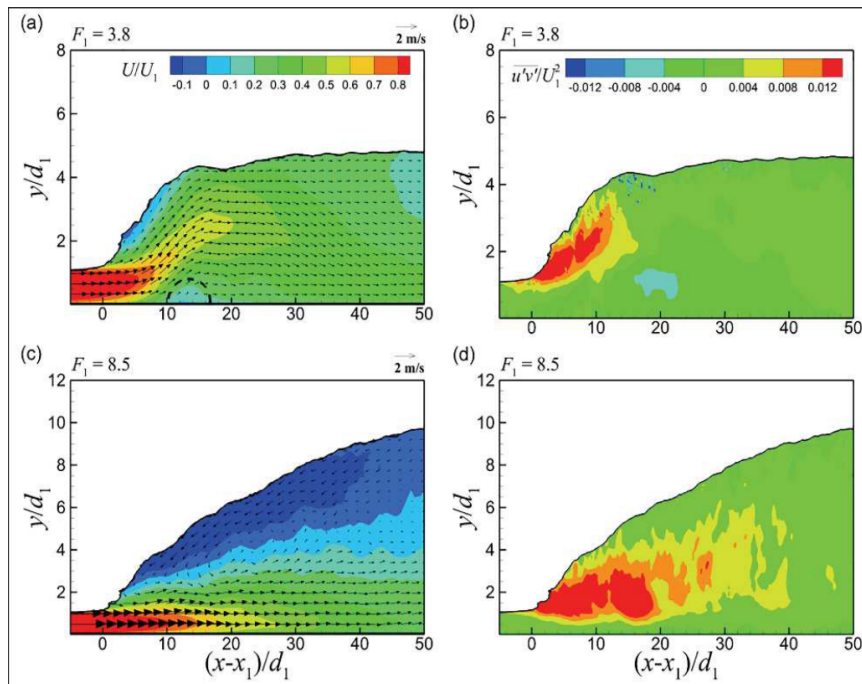


Figure 21 – Contours of (a)-(c) mean streamwise velocity and (b)-(d) Reynolds shear stress of hydraulic jumps over flat beds, from an instantaneous snapshot produced by numerical simulations. Plots (a)-(b) correspond to an oscillating jump while plots (c)-(d) correspond to a stable hydraulic jump. Taken from Jesudhas *et al.*, 2018.

does not translate directly to symmetry in the momentum equation because, for incompressible flows, conservation of energy and momentum are independent from each other. This can easily be inferred from the specific energy equation for a streamline:

$$E_i = y_i + \alpha \frac{u_i^2}{2g},$$

where no coupling with the governing equations of fluid flow is needed to obtain the local energy at a certain point.

To restate, it is not said that self-similarity in energy (which reduces to the generalized Bernoulli equation) also applies for fields *calculated* from the momentum equation: the experiments conducted by Peterka, 1964 show excellent agreement with Belang er’s equation (which is derived from momentum and energy arguments); how-

ever, the Author make the remark that the flow transitions through different states (according to the location of the toe of the jump), in connection with the hydraulic jump types shown in Figure 18, exhibit local non-similarity. This is also confirmed by the numerical experiments of Jesudhas *et al.*, 2018 which also show local non-similarities in the surface roller of hydraulic jumps in the oscillating and stable regimes, as depicted in Figure 21. Notice there that the surface roller is barely present in the oscillating regime whereas for a stable hydraulic jump it is present. Finally, self-similarity of the Reynolds stresses was shown not to hold for hydraulic jumps in the DNS studies conducted by Mortazavi *et al.*, 2014. This seemingly counter-intuitive behaviour of oscillating and weak hydraulic jumps, exhibiting weak rollers and non-similarity, may be unknown to some practitioners when confronted with high-resolution data.

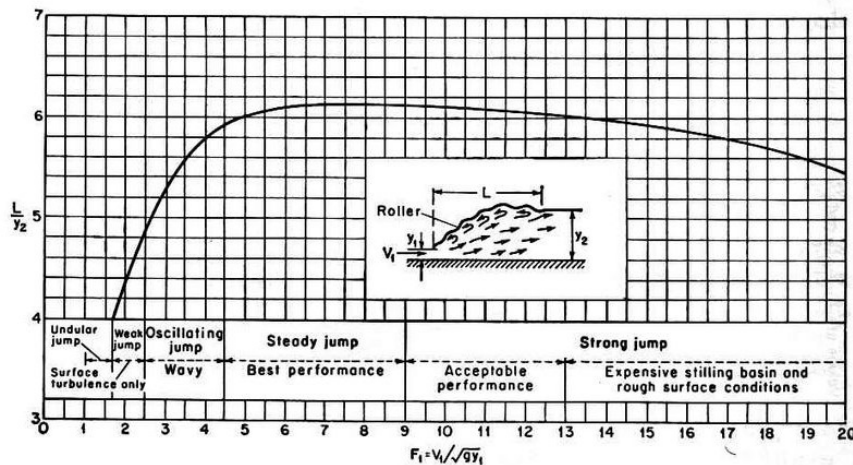


Figure 22 – Length in terms of sequent depth  $y_2$  in horizontal channels. Notice that the suggested range for design is  $4.5 < F_1 < 9$ . Taken from Peterka, 1964.

The experiments conducted by Peterka, 1964 and references therein should be considered a complete compendium of the *hydraulics* of hydraulic jumps, that is, what a practitioner needs to know about hydraulic jumps in order to build structures around dams and rapids. In such cases, the engineer is usually confronted with stable hydraulic jumps types ( $F_1 > 4.5$ ) which, for the most part, are very well understood and even highly suggested- to be used during design stages (see Figure 22). Very seldom is the engineer required (or interested) to work with varied flows where the Froude number approaches unity or with weak-to-oscillating jumps ( $F_1 < 4$ ), except in hydraulic controls; in fact, many reference texts discourage the design of channels with varied flows that range between  $0.8 < F < 1.5$ , given the oscillatory behaviour of around-to-critical flows. Furthermore, the desirable energy dissipation and turbulence mixing properties of hydraulic jumps are better used for incoming flows with high Froude numbers.

## A1.2 Onset of flow separation in weak and oscillating hydraulic jumps: basics

The onset of flow separation on a flat plate (or channel for that matter) is predicated by *adverse* pressure gradients or, broadly speaking, by flow decelerations along the direction of flow. In the case of free-surface-varying open channel flows along horizontal channels, the following three scenarios might exhibit flow separation:

1. a sudden increase in the water height in the channel,
2. a sudden decrease in the water height in the channel,
3. and no water surface variation in the channel.

These need to be inspected in order to determine what conditions may trigger the onset of flow separation. From the possible types of free-surface flows happening in the aforementioned scenarios, only the ones where

there is a net loss of specific energy will be considered. To that end, the second-law of Newton may come handy (neglect friction):

$$\frac{D(\rho\mathbf{u})}{Dt} = \sum_{x,y,z} \mathbf{F} : \quad (23)$$

$$\iiint \frac{\partial(\rho\mathbf{u})}{\partial t} d\Omega + \iint \rho\mathbf{u}\mathbf{u} \cdot d\mathbf{A} = \iint p d\mathbf{A} + \sum_{x,y,z} \mathbf{F}_{\text{external}} \cdot \quad (24)$$

From this Equation, any negative local acceleration resulting from the balance of forces around a control volume suggests the onset of flow separation. Here, the only specific-energy loss mechanism considered is through variations in the channel's cross section. For a constant discharge and subcritical flow, Equation 24 predicates decelerations (the first term on lhs of equation 24 becomes negative, given that the flow is *bulking*) whenever the massic fluxes of momentum become less than the sum of the pressure forces at either end of the control volume, that is, whenever the channel section widens and the water level increases. In this case the seemingly unbalanced deceleration must be balanced by “internal” forces which come in the form of lateral recirculations, as expected in channel expansions. On the other hand, a channel contraction in super-critical flows does not lead to adverse pressure gradients, or decelerations, despite the loss of inertia caused by the contraction; this is because such deceleration is met by lateral external forces produced by the contracted walls, included in the right-hand side of Equation 24.

Finally for the third scenario one possible way to decelerate the flow along the direction of the flow is to have a negative density gradient in the direction of the flow. This might happen in flows undergoing *aeration*. Another possible way is when a *drowned* hydraulic jump occurs: water heights both before and after the jump may be considered equal, and where the start and the length of the roller is imposed by the upstream and downstream hydraulic controls, respectively. This implies that the longer, and weaker, the roller becomes (for example, by increasing the downstream water level) it is more likely to have flow separation in view from Equation 24.

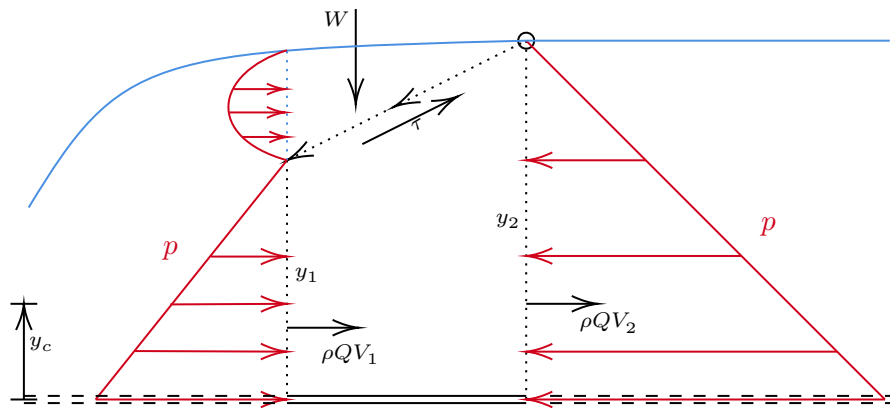


Figure 23 – Control volume, delineated by the black dotted lines, indicating the forces acting on a hydraulic jump in the subcritical region. Notice the upper dotted line represents the outer-most streamline of the surface roller. The circle symbol denotes the end of the surface roller, which enters in contact with the atmosphere.

Separation in a hydraulic jump may be approached in the same way as just done for a channel undergoing contractions or expansions. In this case, however, a careful selection of the control volume may eliminate the local acceleration derivative from Equation 24 but will require a description of the forces that otherwise will be acting *internally* in the roller region. A sketch of the forces acting below the surface roller wedge is depicted in Figure 23. A simple force balance in the direction of the flow following Equation 24 on the control volume comprising the wedge, assuming that the shear region has a slope of approximately 1-to-6 (Rouse *et al.*, 1959), can be written as follows:

$$\tau L \cos(\pi/19) = W / \sin(\pi/19) - \iint \rho\mathbf{u}\mathbf{u} \cdot d\mathbf{A} + \iint p d\mathbf{A}, \quad (25)$$

where  $L$  is the length of the domain. From the diagram, if a surface roller indeed exists, it is clear that the rightmost two terms on the rhs of equation 25 (momentum fluxes and pressure forces) decelerate the flow by virtue of:

1. the net flux of momentum being opposite to the direction of the flow ( $\rho QV_2 < \rho QV_1$ ),
2. and the net flux of pressure forces also being in the direction opposite to the flow.

This implies that, as long as the sum of net flux of momentum and the weight contribution is larger than the net flux of pressure,  $\tau$  remains positive (therefore a roller can be sustained). Notice that one may arrive to the same conclusion were the sheared region produced by flow separation instead of a surface roller (in such case, the wedge weight contribution wouldn't exist). However, this is not the case for stable hydraulic jumps where it seems energy dissipation via wave breaking (surface roller) is more efficient than local flow separation. In general, one may conclude that the net deceleration produced by diverse fluxes at the boundaries of a control volume within a hydraulic jump have to be met by an internal shearing force manifesting in a sort of roller, not necessarily superficial.

It is clear, however, from previous discussions that oscillating-to-weak hydraulic jumps may or may not exhibit intermittent rollers, and flow streamline and free-surface wiggling across the section of analysis. Said intermittent surface rollers may form if the standing wave is strong enough *to break*, that is, to come onto itself and form a breaking standing wave. If the standing wave doesn't have sufficient energy to break, then wiggly streamline patterns will follow. Notice that during these intermittent and "wiggly" patterns the curved (wiggly) flow streamlines respond to a deceleration produced by locally unbalanced *adverse* pressure gradient produced by the curvature of said streamlines. Finally, in the presence of negligible net momentum fluxes, the aforementioned adverse pressure gradient can only be met by a shearing force produced by *flow separation* (remember wave breaking is not possible, hence no surface roller).

### A1.3 Onset of flow separation in weak and oscillating hydraulic jumps: empirical and numerical evidence

The previous discussion laid the "conditions" whereby the onset of flow separation in the bottom of a hydraulic jump may occur: (1) a weak surface roller, and (2) highly curved streamlines. Those two conditions are most probably met in weak and oscillating hydraulic jumps. For the latter case, the high-resolution numerical study of Jesudhas *et al.*, 2018 shows the occurrence of weak flow separation in oscillating jumps, as indicated by the circled region in Figure 21-a. Notice also there that the surface roller is barely present and the flow jet tends to lift upwards with the free-surface. Such lift-off may induce radial accelerations that reduce the dynamic pressure locally, unducing adverse pressure gradients. Additionally, direct numerical simulations of weak hydraulic jumps ( $F_1 = 2$ ) confirm very weak time-averaged surface rollers (Mortazavi *et al.*, 2014; Mukha *et al.*, 2020) as shown in Figure 24-a. The simulations of Mortazavi *et al.*, 2014 also show that the time-space averaged streamlines curve quite considerably after the toe of the jump for weak hydraulic jumps, as indicated in Figure 24-b. Such tilting is further proof of the reduced pressure distributions within weak and oscillating hydraulic jumps. Note that the aforementioned DNS was conducted for a moving reference frame which implies that the wall effects are missing from the solution, hence the onset of separation cannot be resolved there.

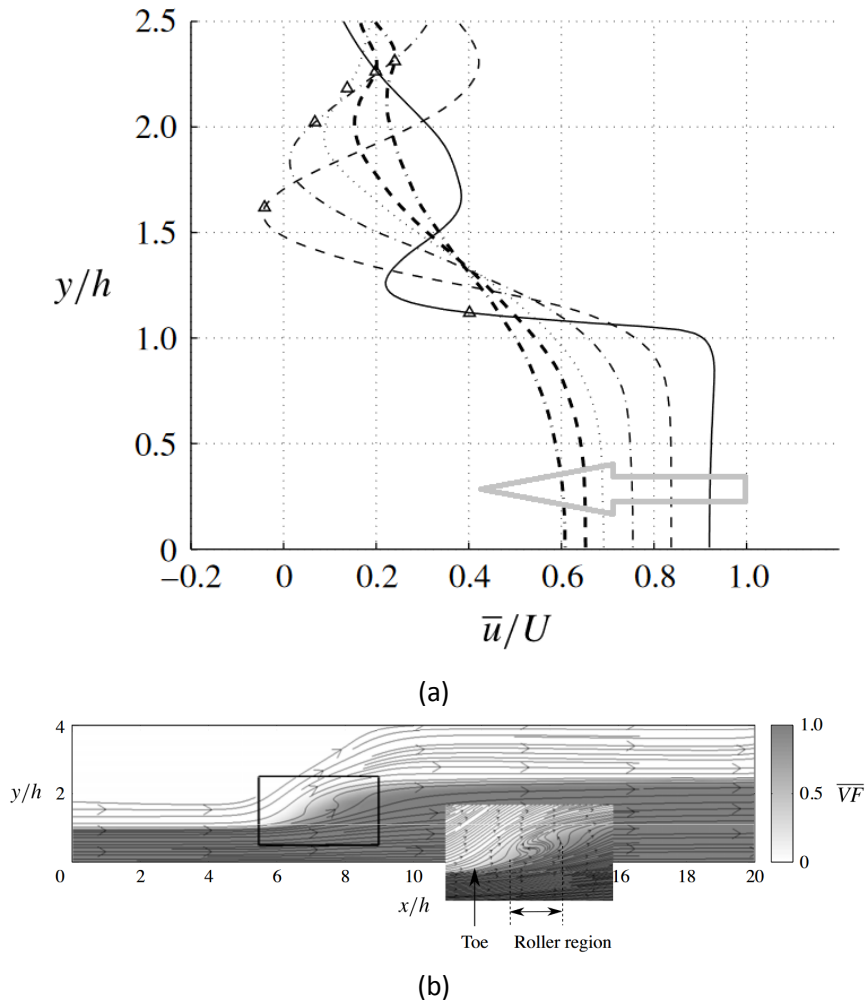


Figure 24 – (a) Non-dimensional streamwise time-averaged velocity profiles after the toe of a hydraulic jump, located at  $x_t$ . The solid line represents the velocity profile exactly at the toe,  $(x - x_f)/h_j = 0$ , and each subsequent line correspond to unit increments (1, 2, 3, ...). The triangle symbol shows the location of the free-surface and the arrow indicate the direction of unit increments. (b) Surface streamlines for time- and spanwise-averaged solution of a weak hydraulic jump. The field VF stands for volume-fraction. Taken from Mortazavi *et al.*, 2014.



## References

- Aupoix, B.; Spalart, P.** (2003). Extensions of the Spalart–Allmaras turbulence model to account for wall roughness. *International Journal of Heat and Fluid Flow* 24 (4): 454–462 pp.
- Bakhmeteff, B. A.; Matzke, A. E.** (1936). The hydraulic jump in terms of dynamic similarity. *Transactions of the American Society of Civil Engineers* 101 (1): 630–647 pp.
- Bayón, A.; Macián-Pérez, J. F.; Vallés-Morán, F. J.; López-Jiménez, P. A.** (2019). EFFECT OF RANS TURBULENCE MODEL IN HYDRAULIC JUMP CFD SIMULATIONS. en. *in*: 1912–1920 pp. DOI: 10.3850/38WC092019-0918
- De Schrijver, C.** (2021). Validatie van CFD-simulaties van een watersprong aan de teen van een overlooppdijk met schaalmodelmetingen. (mathesis). KU Leuven (Campus Bruges): Bruges, BE
- Deshpande, S. S.; Anumolu, L.; Trujillo, M. F.** (2012). Evaluating the performance of the two-phase flow solver interFoam. en. *Computational Science & Discovery* 5 (1): 014016 pp. DOI: 10.1088/1749-4699/5/1/014016
- Devolder, B.; Rauwoens, P.; Troch, P.** (2017). Application of a buoyancy-modified k- $\omega$  SST turbulence model to simulate wave run-up around a monopile subjected to regular waves using OpenFOAM®. en. *Coastal Engineering* 125: 81–94 pp. DOI: 10.1016/j.coastaleng.2017.04.004
- Hornung, H. G.; Willert, C.; Turner, S.** (1995). The flow field downstream of a hydraulic jump. en. *Journal of Fluid Mechanics* 287: 299–316 pp. DOI: 10.1017/S0022112095000966
- Jesudhas, V.; Murzyn, F.; Balachandar, R.** (2018). IDDES Evaluation of Oscillating Hydraulic Jumps. *E3S Web of Conferences* 40: 05067 pp. DOI: 10.1051/e3sconf/20184005067
- Larsen, B. E.; Fuhrman, D. R.** (2018). On the over-production of turbulence beneath surface waves in Reynolds-averaged Navier-Stokes models. eng. *J. Fluid Mech.* 853: 419–460 pp. DOI: 10.1017/jfm.2018.577
- López Castaño, S.; Verelst, K.; Hoydonck, W. van; Mostaert, F.** (2021). On the accurate resolution of hydraulic jumps in OpenFOAM: Measurement techniques for the study of hydraulic jumps. *techreport*, WL2021P20-035-1. Flanders Hydraulics: Borgerhout, Antwerpen (BE)
- Macián-Pérez, J. F.; Vallés-Morán, F. J.; Sánchez-Gómez, S.; De-Rossi-Estrada, M.; García-Bartual, R.** (2020). Experimental Characterization of the Hydraulic Jump Profile and Velocity Distribution in a Stilling Basin Physical Model. *Water* 12 (6). DOI: 10.3390/w12061758
- Madabhushi, R. K.; Vanka, S.** (1991). Large eddy simulation of turbulence-driven secondary flow in a square duct. *Physics of Fluids A: Fluid Dynamics* 3 (11): 2734–2745 pp.
- McCorquodale, J. A.; Khalifa, A.** (1983). Internal Flow in Hydraulic Jumps. en. *Journal of Hydraulic Engineering* 109 (5): 684–701 pp. DOI: 10.1061/(ASCE)0733-9429(1983)109:5(684)
- Menter, F. R.; Egorov, Y.** (2010). The Scale-Adaptive Simulation Method for Unsteady Turbulent Flow Predictions. Part 1: Theory and Model Description. en. *Flow, Turbulence and Combustion* 85 (1): 113–138 pp. DOI: 10.1007/s10494-010-9264-5

- Menter, F.; Egorov, Y.** (2005). A Scale Adaptive Simulation Model using Two-Equation Models. en. *in: 43rd AIAA Aerospace Sciences Meeting and Exhibit*. American Institute of Aeronautics and Astronautics: Reno, Nevada. ISBN: 978-1-62410-064-2. DOI: 10.2514/6.2005-1095
- Menter, F. R.** (1992). Influence of freestream values on k-omega turbulence model predictions. *AIAA journal* 30 (6): 1657–1659 pp.
- Mortazavi, M.; Le Chenadec, V.; Mani, A.** (2014). Numerical simulation of a turbulent hydraulic jump: Characterization of the free interface and large bubble structure. *Centre for Turbulence Research Annual Research Briefs*
- Mukha, T.; Almeland, S. K.; Bensow, R. E.** (2020). LES of a classical hydraulic jump: Influence of modelling parameters on the predictive accuracy. *arXiv:2007.01729 [physics]*. arXiv: 2007.01729
- Ohtsu, I.; Yasuda, Y.** (1991). Hydraulic Jump in Sloping Channels. en. *J. Hydraul. Eng.* 117: 17 pp.
- Park, I.; Kim, K.; Kim, J.; Van, S.** (2009). A volume-of-fluid method for incompressible free surface flows. *International Journal for Numerical Methods in Fluids* 61 (12): 1331–1362 pp.
- Peterka, A.** (1964). Hydraulic design of stilling basins and energy dissipators. 25. US Department of the Interior, Bureau of Reclamation
- Rajaratnam, N.; Subramanya, K.** (1968). Profile of the hydraulic jump. *Journal of the Hydraulics Division* 94 (3): 663–674 pp.
- Rouse, H.; Siao, T. T.; Nagaratnam, S.** (1959). Turbulence characteristics of the hydraulic jump. *Transactions of the American Society of Civil Engineers* 124 (1): 926–950 pp.
- Ubbink, O.; Issa, R.** (1999). A method for capturing sharp fluid interfaces on arbitrary meshes. *Journal of computational physics* 153 (1): 26–50 pp.
- Umlauf, L.; Burchard, H.; Hutter, K.** (2003). Extending the k- $\omega$  turbulence model towards oceanic applications. en. *Ocean Modelling* 5 (3): 195–218 pp. DOI: 10.1016/S1463-5003(02)00039-2
- Wang, H.; Chanson, H.** (2016). Self-similarity and scale effects in physical modelling of hydraulic jump roller dynamics, air entrainment and turbulent scales. en. *Environmental Fluid Mechanics* 16 (6): 1087–1110 pp. DOI: 10.1007/s10652-016-9466-z
- Witt, A.; Gulliver, J. S.; Shen, L.** (2018). Numerical investigation of vorticity and bubble clustering in an air entraining hydraulic jump. en. *Computers & Fluids* 172: 162–180 pp. DOI: 10.1016/j.compfluid.2018.06.019
- Wu, S.; Rajaratnam, N.** (1995). Free jumps, submerged jumps and wall jets. *Journal of Hydraulic Research* 33 (2): 197–212 pp.



DEPARTMENT **MOBILITY & PUBLIC WORKS**  
Flanders Hydraulics

Berchemlei 115, 2140 Antwerp

**T** +32 (0)3 224 60 35

**F** +32 (0)3 224 60 36

[waterbouwkundiglabo@vlaanderen.be](mailto:waterbouwkundiglabo@vlaanderen.be)

[www.flandershydraulics.be](http://www.flandershydraulics.be)